Dynamics of Atmospheres and Oceans 52 (2011) 20–50

Contents lists available at ScienceDirect

Dynamics of Atmospheres and Oceans

journal homepage: www.elsevier.com/locate/dynatmoce

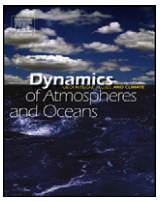

Laboratory and numerical simulations of gravity-driven coastal currents: Departures from geostrophic theory

S.O. Gregorio[a], D.B. Haidvogel[b,*], P.J. Thomas[a], E.S. Taskinoglu[c], A.J. Skeen[d]

[a] Fluid Dynamics Research Centre, University of Warwick, Coventry CV4 7AL, UK
[b] Institute of Marine and Coastal Sciences, Rutgers University, 71 Dudley Road, New Brunswick, NJ 08901, USA
[c] SRA International, Inc., 1201 New Road, Linwood, NJ 08221, USA
[d] Etalon Research Ltd., The TechnoCentre, Coventry CV1 2TT, UK

ARTICLE INFO

Available online 10 May 2011

Keywords:
Rotating flows
Buoyancy-driven plumes

ABSTRACT

Laboratory realizations and numerical simulations of buoyant, gravity-driven coastal plumes are summarized and compared to the inviscid geostrophic theory of Thomas and Linden (2007). The lengths, widths and velocities of the buoyant currents, as well as their internal structure and dynamics, are studied. Agreement between the laboratory and numerical experiments and the geostrophic theory is found to depend on two non-dimensional parameters which characterize, respectively, the steepness of the plumes isopycnal interface (I) and the strength of horizontal viscous forces (Ek_H, the horizontal Ekman number). In general, the numerical and laboratory experiments are in good agreement when conducted at comparable values of I and Ek_H. The best agreement between experiments (both laboratory and numerical) and the geostrophic theory are found for the least viscous flows, though important departures from the theoretical predictions are nonetheless found, particularly in the early development of the plume system. At elevated values of the horizontal Ekman number, laboratory and numerical experiments depart more significantly from theory, e.g., in the rate of plume movement along the coast. A simple extension to the geostrophic theory suggests that the discrepancy between the theoretical and experimental propagation speed should be proportional to the square root of the horizontal Ekman number. The numerical simulations confirm this relationship. For some combinations of the non-dimensional parameters, instabilities develop in the seaward edge of the buoyant plumes.

* Corresponding author. Tel.: +1 732 932 6555x256; fax: +1 732 932 8578.
E-mail addresses: sandy.gregorio@googlemail.com (S.O. Gregorio), dale@imcs.marine.rutgers.edu (D.B. Haidvogel), Eddy.DeCay@eng.warwick.ac.uk (P.J. Thomas), ezgi.ctr.oztekin@faa.gov (E.S. Taskinoglu), ajskeen@gmail.com (A.J. Skeen).

0377-0265/$ – see front matter
doi:10.1016/j.dynatmoce.2011.04.002

The laboratory and numerical experiments are used together to infer the region within parameter space within which the instabilities occur. Mixing of ambient and buoyant fluids by the plume-edge instabilities is explored using the numerical results.

1. Introduction

An important objective in physical oceanography is to understand the dynamics of buoyant discharge and mixing in the coastal ocean. Buoyant fluid entering the coastal ocean from, for example, an estuary will typically form a buoyancy-driven coastal current. The flow develops as a consequence of the density difference between the discharged, buoyant freshwater and the denser, more saline ocean water, in the presence of rotation. Such flows are a major source of nutrients, sediments and contaminants to coastal waters, and may help to support diverse and productive ecosystems. Examples of buoyancy-driven coastal currents include the Columbia River Plume (Hickey et al., 1998), the Delaware Coastal Current (Munchow and Garvine, 1993a,b), the Hudson River outflow (Chant et al., 2008) and the Algerian Current (Obaton et al., 2000), among others. The reader is referred to Chant (2011) for a detailed review of observed systems and their properties.

Garvine (1995) developed a classification of buoyant outflows as either "small-scale" or "large-scale" dependent upon the cross-shore Kelvin number, K, the ratio of the plume width to the baroclinic Rossby radius. "Small-scale" outflows, with Kelvin numbers less than one, are those in which inertial effects are more important than rotation, and outflows tend to spread laterally and to be trapped by advection near the source. "Large-scale" outflows have Kelvin number of order one or greater; such outflows are dominated by the Earth's rotation and form coastally trapped currents that flow in the direction of Kelvin wave propagation. It is this latter category with which we are concerned here.

Prior laboratory studies have investigated such currents, their properties, and the dynamical factors controlling them. Some laboratory experiments have presented results on the dynamics of coastal currents flowing along vertical walls (Griffiths and Hopfinger, 1983; Thomas and Linden, 2007), inclined coastlines (Whitehead and Chapman, 1986; Lentz and Helfrich, 2002) or continental shelves (Avicola and Huq, 2002).

In the experimental study of Thomas and Linden (2007), the width, depth and the propagation speed of currents moving along a simple vertical wall was determined. The experimental data were compared to their theoretical model based on geostrophy, continuity and conservation of potential vorticity. The expressions obtained in their theoretical model are similar to those of Avicola and Huq (2002) who derived a model based on the assumption that the frontal dynamics are that of a Margules front. Overall, good agreement between experiments of Thomas and Linden (2007) and their theory was obtained.

Avicola and Huq (2002) and Lentz and Helfrich (2002) distinguished surface-advected gravity currents, independent of the bottom slope, from slope-controlled gravity currents, for which the buoyant water is in contact with the bottom, and bottom friction is important in the establishment of the current. Lentz and Helfrich (2002) also derived scaling relations for the width, depth and velocity of currents flowing along a sloping bottom. Avicola and Huq (2003a) and Horner-Devine et al. (2006) studied in more detail the dynamics of the bulge, while Avicola and Huq (2003b) attempted to explain the role of the bay exit geometry in the formation of the recirculating bulge.

Griffiths and Linden (1981a) studied the stability of an axisymmetric gravity current along a vertical wall. The wavelength and phase velocities of the disturbances observed by Griffiths and Linden (1981a) agree with their baroclinic instability model of two-layer flow, which takes frictional dissipation caused by Ekman layers into account. Griffiths and Linden (1981b) defined θ as the square of the ratio of the internal Rossby radius of deformation to the horizontal length scale of the flow, and δ as the fraction of the total fluid depth occupied by the layer inside the front. They argued that for $\theta \gg 1$ and $\delta > 0.1$, unstable disturbances obtain most of their energy from the potential energy of the flow, while for $\delta < 0.1$, extraction of the kinetic energy from the shear becomes the dominant driving mech-

anism. Chabert D'Hières et al. (1991) investigated the stability of density-driven boundary currents and compared the results with the Algerian current. Rivas et al. (2005) showed that the presence of an inclined bottom stabilises gravity currents.

On the numerical side, many studies focused on the downstream coastal current and found that the coastal current was largely in geostrophic equilibrium. Oey and Mellor (1993) noticed an unsteady plume/front system in their numerical experiments. Chao and Boicourt (1986) divided the plume into two dynamically distinct regions: a bulge region near the estuary mouth and a downstream coastal current. They looked at the dynamics at the river mouth. Chao and Boicourt (1986) found that the nose of the current advances faster in the estuary region than down the coast and suggested that mixing near the estuary mouth was responsible for the slowing down. Csanady (1984) and Wright (1989) simulated a surface-to-bottom density front over a sloping bottom and a flat continental shelf, respectively, and noticed that offshore transport of buoyant water in the bottom boundary layer contributed to the cross-shelf movement of bottom-advected plumes. Chapman and Lentz (1994) showed that this effect moves the front offshore until it reaches the depth where the vertical shear causes a reversal in the cross-shelf flow across the entire base of the front, eliminating the offshore buoyancy flux in the bottom boundary layer. Fong and Geyer (2002) investigated the dynamics of the bulge. They found that in the absence of an ambient flow field, the downstream coastal current carries a portion of the freshwater, while the remaining freshwater recirculates in a continually growing bulge in the vicinity of the estuary mouth. Fong and Geyer (2002) concluded, with the support of another set of numerical simulations, that an external forcing agent (like an ambient current) was required for transporting all the discharged freshwater downstream.

Here, we combine laboratory studies (those of Thomas and Linden (2007) and additional experiments performed at Warwick University by the first author) with numerical simulations to further investigate departures from the geostrophic theory of Thomas and Linden (2007). We pay particular attention to the internal dynamics of the plumes, the occurrence of instabilities within them, and the role of viscous forces in their evolution. The plan of the paper is as follows. In Section 2, we review the methods (theoretical, experimental, numerical) employed. Section 3 uses the new laboratory and numerical studies together to explore the kinematic properties of the buoyancy-driven plumes, and to identify their non-dimensional dependencies. The internal dynamics of the plumes is investigated in section 4. A final section offers a summary and concluding remarks.

2. Methods

Fig. 1, from Chant et al. (2008), illustrates for the case of the Hudson River some of the observed properties of river plumes. Note in particular the presence of the bulge of buoyant water near the estuary mouth and the narrow coastal current emanating from it. The coastal current flows in the direction of Kelvin wave propagation, that is with the coast on its right (Northern Hemisphere). Many additional processes (e.g., wind forcing, coastline irregularities, and bottom boundary layers) may modify the evolution and properties of buoyancy-driven coastal currents (Chant, 2011). Our concern here is with the simple case of a surface-advected plume moving along a straight coastline, in the absence of wind forcing.

2.1. Geostrophic theory

Thomas and Linden (2007) considered currents in a two-layer system flowing along a vertical coastline. Their flow geometry and the nomenclature employed in their analysis are illustrated in Fig. 2.

The curvature of the circular wall is neglected and a Cartesian coordinate systems ($\boldsymbol{x}$, $\boldsymbol{y}$, $\boldsymbol{z}$) is introduced. The origin of the coordinate system coincides with the outlet of the source from which the buoyant freshwater discharges. It is assumed that the velocity components in the y- and z-directions are negligible in comparison to the velocity component in the x-direction. All variations in the x-coordinate direction are also neglected so that $\partial/\partial x = 0$. Therefore $\boldsymbol{u} = (u(y, z), 0, 0)$.

As only processes near the coastal wall are considered, the lowest layer is imagined deep and at rest. Frictional effects are ignored and the current is assumed to be steady and in geostrophic balance;

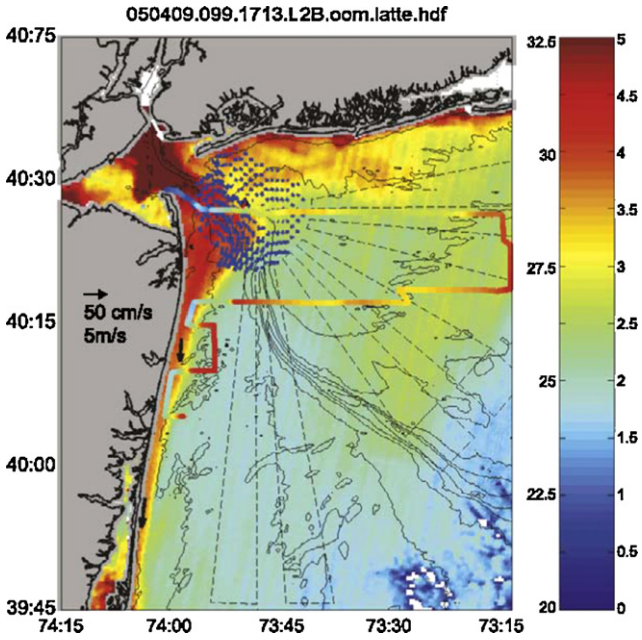

Fig. 1. Hudson river outflow. The image is obtained from *MODIS* at 17:13*GMT*. Blue arrows show *CODAR* field, black from shelf moorings and white from *NOAA* mooring at the Narrows. The color bar (right side) is for surface salinity from shiptrack shown in the figure (from Chant et al., 2008). (For interpretation of the references to color in this figure legend, the reader is referred to the web version of the article.)

that is, the Coriolis acceleration term in the cross-plume direction is balanced by the cross-plume pressure gradient component. The pressure is considered to be hydrostatic, and, as the freshwater is released from a continuous point source, it is further assumed that it is released with zero potential vorticity.

Using conservation of mass, angular momentum and potential vorticity, the analysis in Thomas and Linden (2007) shows that the current width, w_0, its depth, h_0, its length, $l(t)$, and its constant

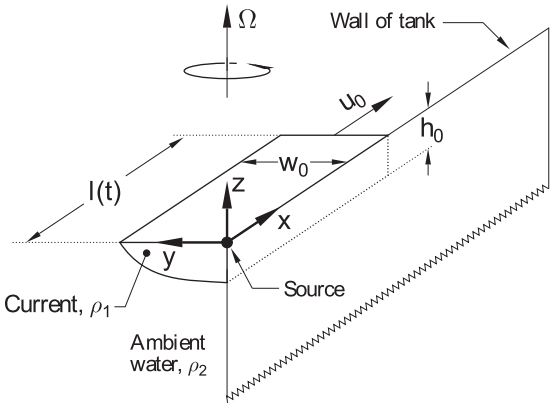

Fig. 2. Sketch illustrating the nomenclature employed to develop the theoretical model for currents flowing along a vertical wall (from Thomas and Linden, 2007).

propagation speed, $u_0 = l/t$, are given respectively by

$$w_0 = \left(\frac{g' q_0}{\Omega^3}\right)^{1/4}, \quad h_0 = \left(\frac{4\Omega q_0}{g'}\right)^{1/2}, \quad l = \frac{3}{4}(q_0 g' \Omega)^{1/4} t, \quad u_0 = \frac{3}{4}(q_0 g' \Omega)^{1/4}. \tag{1}$$

where Ω is the angular rotation rate of the turntable, q_0 is the volumetric rate of the buoyant inflow, and g' is the reduced gravity, defined by

$$g' = \frac{\rho_2 - \rho_1}{\rho_1} g, \tag{2}$$

where $g = 981\ \mathrm{cm\ s^{-2}}$ is the acceleration due to gravity.

As discussed in Thomas and Linden (2007), w_0 is equivalent to the Rossby deformation radius, R_D, based on the depth of the current. The results of (1) can be expressed in dimensionless form by non-dimensionalizing all lengths by w_0 and by introducing the non-dimensional time $T = \Omega t$. Using capital letters to denote non-dimensional variables, one obtains:

$$W = 1, \quad H = 2I^{5/4}, \quad L = \frac{3}{4}T, \quad U_0 = \frac{L}{T} = \frac{3}{4}, \tag{3}$$

where

$$I = \frac{\Omega q_0^{1/5}}{g'^{3/5}} \tag{4}$$

is a dimensionless parameter. Reference to (3) reveals that $H = h_0/w_0$; therefore, the parameter I characterizes the aspect ratio of height to width of the current.

Note that I also characterizes the isopycnal slope separating the two layers. Thomas and Linden (2007) noticed that currents with low values of I, thus currents with a small isopycnal slope, are wide and shallow, while currents with high values of I, thus currents with a large isopycnal slope, are deep and narrow.

The properties of the coastal current are found to be related to the values of several non-dimensional parameters. These include: the horizontal Ekman number, Ek_H,

$$Ek_H = \frac{\nu}{f w_0^2} = \frac{\nu \Omega^{1/2}}{2 q_0^{1/2} g'^{1/2}}, \tag{5}$$

and the vertical Ekman number, Ek_V,

$$Ek_V = \frac{\nu}{f h_0^2} = \frac{\nu g'}{8 \Omega^2 q_0}, \tag{6}$$

using (1) and $\nu = 0.01\ \mathrm{cm^2\ s^{-1}}$ for the kinematic viscosity of water.

2.2. Experimental methods

The goal of the laboratory experiments was to simulate estuarine discharge of buoyant water into an environment of salty, denser ocean water along a vertical coastline. The arrangement of the experimental configuration is shown in Fig. 3.

The experiments were carried out in a circular tank with a radius of 50 cm, placed on a rotating turntable to simulate the rotation of the Earth. The tank was filled with salt water of a specified density ρ_2 representing the ocean water, while freshwater of density ρ_1, with $\rho_1 < \rho_2$, was stored in a separate, co-rotating smaller reservoir mounted on the turntable. The density difference between the freshwater and the salt water was characterized in terms of the reduced gravity, g'.

The source for these experiments was a pipe with a diameter of 1 cm, which was adjusted to be level with the surface of the dense salt water. The buoyant outflow was released continuously, with a constant specific volumetric discharge rate q_0. The fluid was discharged vertically upwards, rather than horizontally as would be the case in the natural environment. The purpose of the vertical discharge

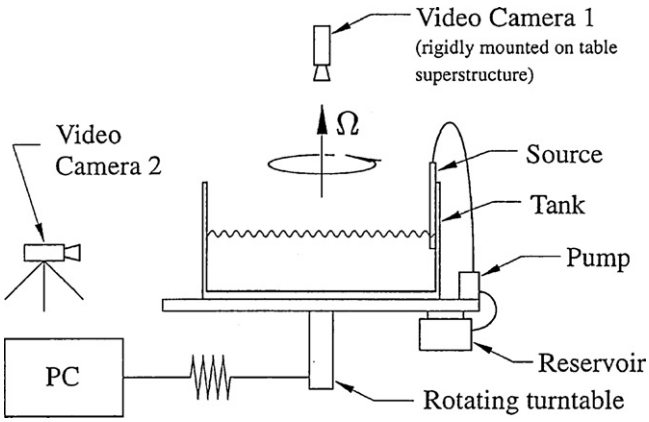

Fig. 3. Sketch of the experimental setup (from Thomas and Linden, 2007).

direction was to minimize momentum flux effects and mixing of freshwater and salt water near the source.

The depth of the salt water was sufficient so the current was not affected by the bottom of the tank. The turntable was set to a specified rotation rate Ω before each experiment, and the ambient ocean fluid was allowed to reach solid body rotation before each experiment was begun. At the end of each experiment, the ratio between the volume of input fluid and the ambient water already in the tank was less than 0.064 and the tank level rose no more than 5 mm.

The buoyant outflow was marked using small concentrations of food coloring, while the ambient water was clear, in order to facilitate flow visualization of the coastal current. One video camera was rigidly mounted on the rotating turntable and filmed the current through a large mirror mounted at the top of the tank. A second video camera was positioned next to the turntable and filmed the flow through the transparent sidewall of the tank.

In total, three parameters were varied for these experiments: the rotation rate, Ω, the volumetric flow rate at the source, q_0, and the reduced gravity, g'. More details on the set-up of these experiments and the results obtained can be found in Thomas and Linden (2007).

The coastal current width was not inferred from dye concentrations, as dye concentrations can vary from experiment to experiment. Also, the use of dye concentrations to infer width is ambiguous because dye may occupy regions that are not dynamically active (e.g., dye may be advected or mixed to a region in which the velocities and pressure gradients are small) (Avicola and Huq, 2002). Thomas and Linden (2007) discuss in more detail in their Section 3.5 why dye measurements are not a good indicator for current width and give error estimates for the dye measurement of the current width.

Here, measurements of the coastal current width and its surface velocities are made using a 2-component Particle Image Velocimetry (*PIV*) system. The *PIV* camera was fitted with a *f*:1.4 50 mm lens, and it was aimed upwards at the large mirror mounted at the top of the tank. Using this arrangement, approximately the entire half of the water surface could be viewed. A stroboscope was mounted also at the top of the tank, aimed directly towards the area being viewed by the camera. Both devices were triggered by a *microPulse* timing generator, under the control of *proControl* software (*Etalon Research Ltd.*). This allowed simple adjustment of the inter-frame pulsing period (Δt), with values of between 80 and 190 ms being used for the majority of the experiments.

White polyamide seeding particles with 100 μm diameter were mixed into the ambient salt water, then allowed to float on top of the surface water. The freshwater was free from particles as they would obstruct the source outlet. The salt water was dyed dark blue using food coloring to get a good contrast between particles and background.

Experiments utilizing *PIV* methods were conducted by the first author at Warwick University. The fifth author provided the *PIV* camera and associated software, and helped with the data processing. The *PIV* experimental parameters are listed in Table 1.

Table 1
Experimental parameters of the *PIV* small-scale laboratory experiments. The values, listed in order, are the Coriolis parameter, f (s^{-1}), the reduced gravity anomaly, g' ($cm\,s^{-2}$), the averaged flow rate, q_0 ($cm^3\,s^{-1}$), the ambient ocean depth, H_D (cm), the dimensionless parameter, I, the horizontal Ekman number, Ek_H, and the vertical Ekman number, Ek_V.

Lab. Exp.	J01	J02	J03	J04	J05
f	2.05	2.09	2.13	1	1.01
g'	2.99	2.99	2.99	2.99	2.99
q_0	3.21	19.99	28.28	3.21	19.99
H_D	9.8	10.1	10.2	10.3	10.3
I	0.67	0.988	1.076	0.328	0.478
Ek_H	1.63×10^{-3}	6.62×10^{-4}	5.61×10^{-4}	1.14×10^{-3}	4.6×10^{-4}
Ek_V	1.11×10^{-3}	1.71×10^{-4}	1.17×10^{-4}	4.64×10^{-3}	7.27×10^{-4}
Lab. Exp.	J06	J07	J08	J09	J10
f	2.04	2.1	1	1	1.01
g'	18.66	18.65	18.63	18.62	18.61
q_0	3.21	19.99	3.21	19.99	28.28
H_D	10.2	10.2	10.1	10.2	10.3
I	0.222	0.331	0.109	0.157	0.171
Ek_H	6.52×10^{-4}	2.65×10^{-4}	4.58×10^{-4}	1.83×10^{-4}	1.55×10^{-4}
Ek_V	7×10^{-3}	1.06×10^{-3}	2.89×10^{-2}	4.66×10^{-3}	3.21×10^{-3}

2.3. Numerical methods

The circulation model used in this study is the Regional Ocean Modeling System (*ROMS*, http://marine.rutgers.edu/po/index.php?model=roms), which has been developed and is supported by a consortium of institutions including Rutgers University and *UCLA*[1]. *ROMS* has been developed for, and applied to, a wide variety of coastal marine applications, including studies of buoyancy-driven coastal currents (e.g., the idealized studies of the Hudson River by Zhang et al. (2009) and the realistic simulations of the Columbia River plume by Liu et al. (2009)).

ROMS utilizes consistent temporal averaging of the barotropic mode to guarantee both exact conservation and constancy preservation properties for tracers and therefore more accurately resolves barotropic processes, while preventing aliasing of unresolved barotropic signals into the slow baroclinic motions. Accuracy of the mode-splitting is further enhanced due to redefined barotropic pressure-gradient terms to account for the local variations in the density field (i.e., the pressure-gradient truncation error is greatly reduced). Vertical interpolation is based on conservative parabolic splines. Finally, *ROMS* uses orthogonal curvilinear coordinates in the horizontal, an essential feature here, as described below. Shchepetkin and McWilliams (2005) describe in detail the algorithms that comprise the ROMS computational kernel, and Haidvogel et al. (2007) discuss the validation of ROMS in a variety of oceanic settings.

The *ROMS* model employs the hydrostatic approximation in the vertical equation of motion, traditional in models of the large-scale ocean circulation. This assumption is not problematic, as we are working in a rotationally dominated regime. However it does introduce one complication. This has to do with the method of injection of buoyant fluid. In the laboratory setting, this is accomplished via direct vertical insertion. This option is not readily available to *ROMS*, wherein the hydrostatic assumption precludes independent specification of vertical fluid motion.

In configuring *ROMS* for these simulations, several alternatives were therefore considered for introduction of buoyancy. These options included the addition of light fluid via a specified rain field, the use of nudging (a relaxation term in the density equation), and horizontal injection of light fluid via an attached estuary. A hybrid of the latter two approaches was eventually adopted, as shown schematically in Fig. 4.

The annular geometry of the laboratory experiments is reproduced easily in *ROMS* by choosing a polar coordinate system, and adopting periodic boundary conditions at the matching edge in the

[1] University of California, Los Angeles, USA.

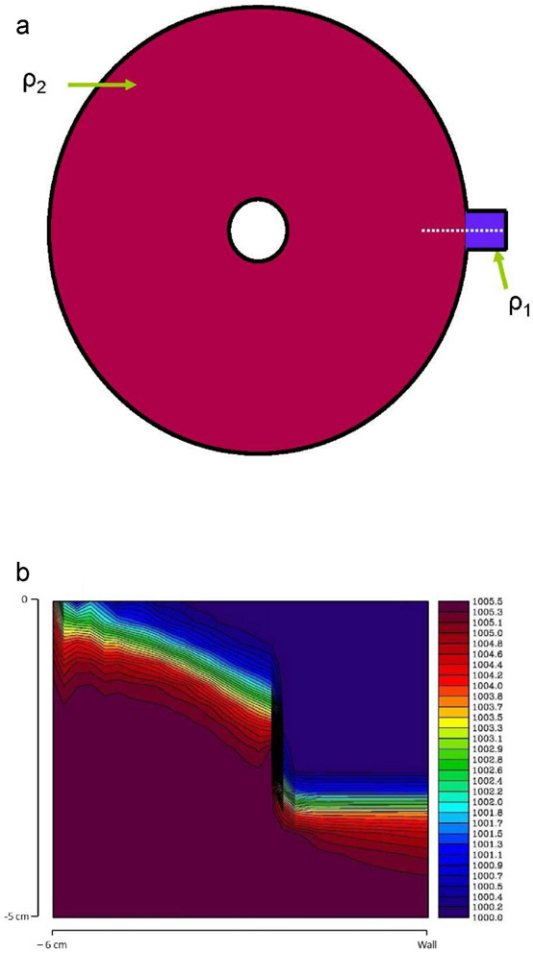

Fig. 4. *ROMS* configuration. (a) Top view of the ROMS configuration. (b) Vertical section of density taken along the dashed line in Fig. 4a. The *x*-axis is along the radial direction, and the *y*-axis is along the vertical direction. Color bar is for density (in kg m^{-3}). Only the upper 5 cm of the water column is shown.

azimuthal direction. A singularity at the center of the circle is avoided by cutting away a small section in the center, yielding a donut shape (Fig. 4(a)). A small estuary containing buoyant (density ρ_1) fluid at the surface, is attached to the sidewall of the donut which is itself initially filled with denser fluid ($\rho_2 > \rho_1$). A strong nudging term within the estuary (but not within the annulus!) maintains a supply of light water within the estuary throughout the simulation.

For consistency with the laboratory experiments, in which no horizontal momentum is introduced with the light water, we allow the injection of buoyant fluid in *ROMS* to take place by gravitational adjustment. At the initial instant, there exists a vertical density front between the cap of fresh water in the estuary and the adjacent dense water in the annulus. This front is gravitationally unstable and, once allowed to evolve in time, slumps into the annulus, producing a source of buoyancy just outside the mouth of the estuary[2] (Fig. 4(b)). The rate of buoyancy injection (i.e., the analogue of q_0 in the

[2] Note that there is no net source of mass, as in the laboratory setting. Buoyant fluid is discharged from the estuary at the surface and denser ambient water enters the estuary at depth. Surface density in the estuary is kept fresh by the density nudging term.

laboratory frame) is therefore not an independently specified parameter in this approach. However, it may be determined *a posteriori*.[3]

As discussed further below, simulations with *ROMS* were conducted both with and without explicit levels of horizontal viscosity. (The value of diffusivity in the density equation was set to zero in all cases.) The sidewall boundary conditions in the momentum equations are either free-slip (without viscosity) or no-slip (non-zero viscosity). No-flux sidewall boundary conditions are applied in the density equation.

The *ROMS* simulations were conducted at Rutgers University by the second and fourth authors. The numerical solutions are obtained on a polar grid having 128 points (stretched towards the outer annular wall) in the radial direction and 512 points around the circumference; 60 equally spaced levels are used in the vertical direction. The finest resulting grid spacing is of order two millimeters. The required time step used for the simulations was two milliseconds. This is, to our knowledge, the smallest-scale application thus far produced with *ROMS*.

2.4. Data extraction methods

In the next section, we examine the current length, width and velocity obtained in the *ROMS* and laboratory experiments.

The nose displacement of the coastal currents in *ROMS* was extracted from the surface density field, as follows. First, the background density value was subtracted from the surface density field, for each time step. Thus non-zero values of the density anomaly on the surface defined the coastal current. Then, for each time step, the maximum azimuthal location of a negative density anomaly, proceeding in the direction of plume propagation, defined the azimuthal location of the current head. The *ROMS* current length data are compared to the data from Thomas and Linden (2007) (see their paper for data extraction details for the current length).

The width of the coastal currents in *ROMS* was extracted in a similar fashion to the length, that is, from the surface density field. First, the background density value was subtracted from the surface density field, for each time step. Then, at one fixed azimuthal position, for each time step, the maximum radial location of a negative density anomaly, proceeding in the direction of the annulus center, defined the width.

The current width and velocity in the laboratory were extracted using *PIV* methods. The *PIV* measurements produced a time-series of "vector maps", each comprising 2-component velocity measurements, recorded in Cartesian coordinates. 61 radial profiles (each containing 150 samples) were extracted from each map, and the tangential and radial components of velocity at each point along the profile computed. The profiles covered the range $r = 0$–52 cm (the tank radius was 50 cm), with 2° spacing between profiles. Therefore 1/3 of the tank was covered by the *PIV* measurements, with the current source positioned further upstream. The profiles were next grouped into 3 "sectors" (each covering a 40° segment of the tank), and the velocity profiles within each sector averaged. An *FFT* was then calculated using data extracted from the spatially averaged time-series data in order to estimate the frequency of the disturbance introduced by the tank's "sloshing". Finally, the data was smoothed in the time-domain using a sliding-window averaging-filter with size equal to the wavelength of the temporal disturbance.

To obtain the width, one needs to identify the seaward limit of the coastal current. The coastal current was not inferred using the maximum value of the gradient for the azimuthal velocity as any perturbation in the experiment could disturb the measurements with this method. Instead, a reference value for the velocity in the current was chosen and all the values for the velocity above this reference value defined the coastal current. After examination, this value was found to be approximately 30% of the value for the maximum velocity in the current. Current widths measured with this latter method were found to be similar to current width obtained by using the maximum value of the gradient for the azimuthal velocity.

[3] Since the rate of buoyancy injection is not independently prescribed, the values of the parameter I cannot be matched *a priori* to those of the laboratory experiments.

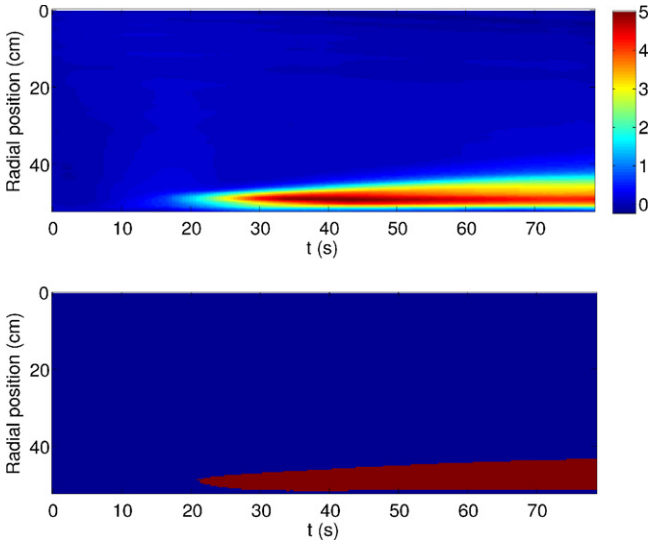

Fig. 5. *PIV* width extraction method (the color bar on the top image is for velocity ($cm\,s^{-1}$)).

Fig. 5 illustrates the width extraction method for the *PIV* experiments. The top image displays the azimuthal velocity for one *PIV* experiment (experiment *J*10 listed in Table 1), measured at a fixed distance downstream from the source, $d_s = 77.5$ cm, as a function of time (the color bar next to the top image is for velocity ($cm\,s^{-1}$)). The *y*-axis represents the radial position. The reference value for the velocity is chosen to be $1.7\,cm\,s^{-1}$; thus all the values for the velocity from the top image above the value of $1.7\,cm\,s^{-1}$ define the coastal current, and are displayed in the bottom image of Fig. 5. The reference value for the velocity of the current from Fig. 5 is found to be ∼34% of the maximum speed, $u_{max} = 5.04\,cm\,s^{-1}$.

2.5. Comparison of the three approaches

The geostrophic theory, the laboratory experiments, and the numerical simulations all differ somewhat in their formulation and assumptions. For example, the theory is for steady, inviscid flow, makes no specification of how the buoyant water is introduced, and ignores bulge formation entirely. The laboratory and numerical models are both able to offer a more complete picture of the combined bulge/coastal current system, but they too differ in several respects, most notably in how they introduce their buoyancy. An interesting issue addressed below is just how robust the plume properties are in the face of these differing methodological choices and assumptions.

3. Kinematic flow features and regimes

The theory of Thomas and Linden (2007) assumes an inviscid ocean. To begin, we therefore configured *ROMS* with zero explicit horizontal viscosity. (By virtue of its spatial and temporal discretization, *ROMS* carries some implicit smoothing. It is therefore possible to conduct simulations with explicit values of horizontal viscosity and diffusivity set to zero. The issue of mixing in these simulations is discussed below in Section 4.) Ten "inviscid" experiments were run. In order to match the laboratory experiments, we also conducted simulations with the lateral viscosity set to the molecular value of $10^{-2}\,cm^2\,s^{-1}$. Seven "viscous" experiments were carried out. These seven numerical simulations precisely duplicate seven of the inviscid simulations, except for the inclusion of lateral viscosity. The parameters for the *ROMS* experiments are summarized in Table 2.

Table 2
Experimental parameters of the *ROMS* simulations: plumes 118–136 have no lateral viscosity while plumes 148–155 have the lateral viscosity set to the molecular value of 10^{-2} cm^2 s^{-1}. The values, listed in order, are the Coriolis parameter, f (s^{-1}), the reduced gravity anomaly, g' (cm s^{-2}), the averaged flow rate, q_0 (cm^3 s^{-1}), the ambient ocean depth, H_D (cm), the dimensionless parameter, I, the horizontal Ekman number, Ek_H, and the vertical Ekman number, Ek_V.

Plume	118	120	125	126	128	130
f	1	1	2	3	3	3
g'	5.4	21.6	5.4	5.4	21.6	43.2
q_0	9	20.97	5.03	3.54	11.12	22.17
H_D	12.5	12.5	12.5	12.5	12.5	12.5
I	0.282	0.145	0.502	0.702	0.384	0.291
Ek_H	0	0	0	0	0	0
Ek_V	3×10^{-3}	5.15×10^{-3}	1.34×10^{-3}	8.47×10^{-4}	1.08×10^{-3}	1.08×10^{-3}

Plume	131	132	134	136	148 (126)	149 (131)
f	1	2	2	3	3	1
g'	43.2	43.2	21.6	32.4	5.4	43.2
q_0	30.54	28.97	15.91	10.27	3.5	31.23
H_D	12.5	12.5	12.5	3	12.5	12.5
I	0.103	0.205	0.275	0.297	0.701	0.104
Ek_H	0	0	0	0	1.41×10^{-3}	9.63×10^{-5}
Ek_V	7.07×10^{-3}	1.86×10^{-3}	1.7×10^{-3}	1.75×10^{-3}	8.57×10^{-4}	6.92×10^{-3}

Plume	150 (134)	151 (125)	152 (118)	153 (128)	155 (130)
f	2	2	1	3	3
g'	21.6	5.4	5.4	21.6	43.2
q_0	16.2	5.04	9.47	12.76	15.97
H_D	12.5	12.5	12.5	12.5	12.5
I	0.276	0.502	0.285	0.395	0.273
Ek_H	2.67×10^{-4}	9.59×10^{-4}	4.94×10^{-4}	3.69×10^{-4}	2.33×10^{-4}
Ek_V	1.67×10^{-3}	1.34×10^{-3}	2.85×10^{-3}	9.4×10^{-4}	1.5×10^{-3}

In this section, we compare these inviscid and viscous numerical simulations with the geostrophic model of Thomas and Linden (2007), their small-scale laboratory experiments, and the *PIV* experiments described in Section 2.2.

3.1. Introductory remarks

As discussed in Section 2.3, *ROMS* internally determines its own buoyancy injection rate, the analogue of q_0.[4] To obtain the value of q_0 for each simulation, we measure the volume-averaged density in the annulus (excluding the estuary) as a function of time, from which an estimate of the rate of buoyancy injection per unit time is obtained.

We can anticipate that the value of q_0 in *ROMS* will depend on the values of the other experimental parameters, the rotation rate, Ω, and the reduced gravity, g'. From Table 2, q_0 is seen to increase as Ω decreases and as g' increases. This self-determined dependence is in fact consistent with the geostrophic scaling of Thomas and Linden (2007), in which the volumetric flow rate is shown to be proportional in the theory to g' and inversely proportional to Ω. Lastly, one can note that the value of the flow rate does not change appreciably by the addition of lateral viscosity.

One final inviscid experiment, number 136, was conducted in which the depth of the annulus/estuary was reduced from 12.5 to 3.0, with no accompanying reduction in the thickness of the freshwater cap in the estuary. The resulting value of q_0 (Table 2) is suggestive of a dependence on depth. However, we have not pursued this possibility.

Fig. 6(a) is a picture of a laboratory experiment from Thomas and Linden (2007), obtained with the video camera mounted on the rotating turntable, which shows a current viewed from above the

[4] Henceforth, we will refer to this simply as q_0.

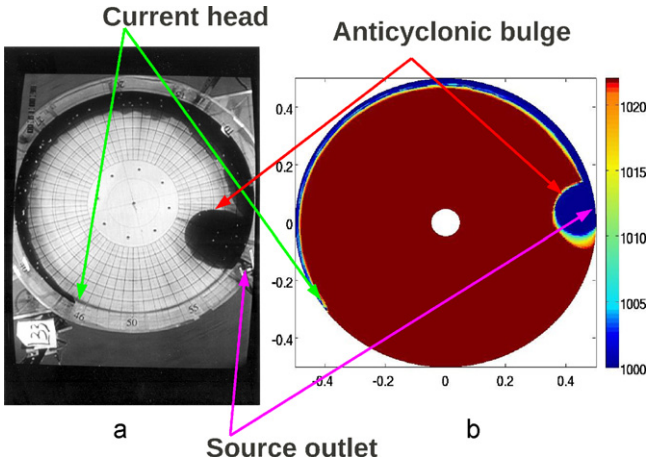

Fig. 6. Top view of a coastal current simulated, (a) in the laboratory, (b) numerically. The images are taken at $T = 30$. $I = 0.301 \pm 0.026$, $Ek_V = (1.4 \pm 0.3) \times 10^{-3}$, *ROMS*: $Ek_H = 0$, Laboratory experiment: $Ek_H = 2.68 \times 10^{-4}$. In (b), color bar is for density(in kg m^{-3}).

circular tank, looking vertically downwards onto the fluid surface. The dyed current fluid appears dark on the picture. Fig. 6(b) is a picture from an inviscid numerical simulation, which displays the density field at the surface. A comparison of the pictures in Fig. 6(a) and (b) reveals a great degree of qualitative similarity. The buoyancy-driven flows are, in both cases, characterized by a stationary "bulge" of fresh water retained near the buoyant outflow, and a propagating plume of fresh water. In both settings, the Coriolis parameter is positive; therefore the turntables rotate cyclonically, as do the plumes, keeping the wall to their right.

In both the laboratory and numerical observations, when the source is turned on a buoyant outflow disperses along the coastline. This outflow can be decomposed into a growing anti-cyclonic bulge and a coastal plume flowing downstream of the bulge. For some experimental parameters combinations, the rate of elongation of the plume shows little decrease during the whole experiment, while for some other experimental parameter combinations, the coastal plume is observed to accelerate at the start of the experiment, then to decelerate to a nearly constant speed. Finally, for some experiments instabilities are seen to form and evolve along the edge of the buoyant plumes. We illustrate these features next, and pursue their dynamical implications below in Section 4.

3.2. Current length

Figs. 7(a) and 8(a) show raw data for the current length, l, as a function of time, t, for the inviscid and viscous numerical experiments, respectively, while Figs. 7(b) and 8(b) redisplay the data in non-dimensional form. In Figs. 7(b) and 8(b), data are non-dimensionalized by w_0 and the solid line superposed on the figures is the theoretical prediction of Thomas and Linden (2007), namely, $L = (3/4)T$. The majority of the numerical experiments were terminated when the current nose got back to the source. The remaining cases – plumes 118, 125, 126, 148 and 152 – were stopped before the plume re-entered the source region.

The experiments of Thomas and Linden (2007) show that the current speed increases when increasing the values of the flow rate, q_0, the rotation rate, Ω, and the reduced gravity, g'. From Figs. 7(a) and 8(a), and from Table 2, increasing the values of g' and q_0 increases the current speed, in agreement with theory.

A comparison between Figs. 7 and 8 reveals that while in Fig. 7 the velocity of all the currents shows little diminution during the plume propagation along the annulus, the current velocity in Fig. 8 is consistently higher in the vicinity of the source than further downstream (as it was also observed in the simulations of Chao and Boicourt (1986)) and currents slow down substantially during the

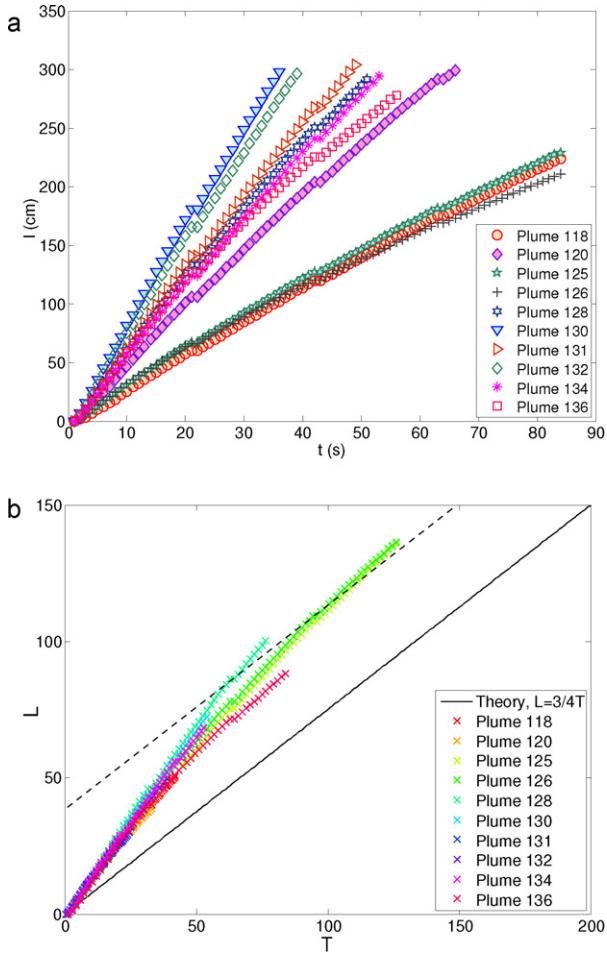

Fig. 7. Nose propagation of the inviscid plumes. (a) Summary of the current length, l, as a function of time, t. (b) Summary of the non-dimensional current length, L, as a function of the non-dimensional time, T. The solid line represents the theoretical prediction, $L = (3/4)T$, of Thomas and Linden (2007). The dashed line is parallel to the theoretical prediction, shifted upwards to facilitate visual comparison with the numerical results.

simulation (especially for the plumes 148 and 151 which have the lowest flow rate, in agreement with the experimental findings of Thomas and Linden (2007)).

Fig. 9 compares the simulations with lateral viscosity to their corresponding inviscid numerical simulations and to the small-scale laboratory experiments and the geostrophic model of Thomas and Linden (2007) for the non-dimensional current length, L. Experiments with similar values for the parameter I, the horizontal and vertical Ekman numbers, Ek_H and Ek_V, respectively, are expected to be analogous. The non-dimensionalizing factor of Ω for the time was different in the *ROMS* and laboratory experiments shown in Fig. 9, thus explaining why the curves of the *ROMS* experiments for the current length are shorter than the curve of the laboratory experiment.

From Figs. 7(b) and 9, two conclusions may be drawn. First, the rate of elongation of the plumes in the inviscid simulations always exceeds the estimate given by the geostrophic theory. Second, the non-dimensional plume lengths in the inviscid simulations are comparable to the laboratory experiments with very low values for the horizontal Ekman number; however plumes from the inviscid simulations have a more rapid rate of elongation than plumes from the laboratory experiments (Fig. 9(a)).

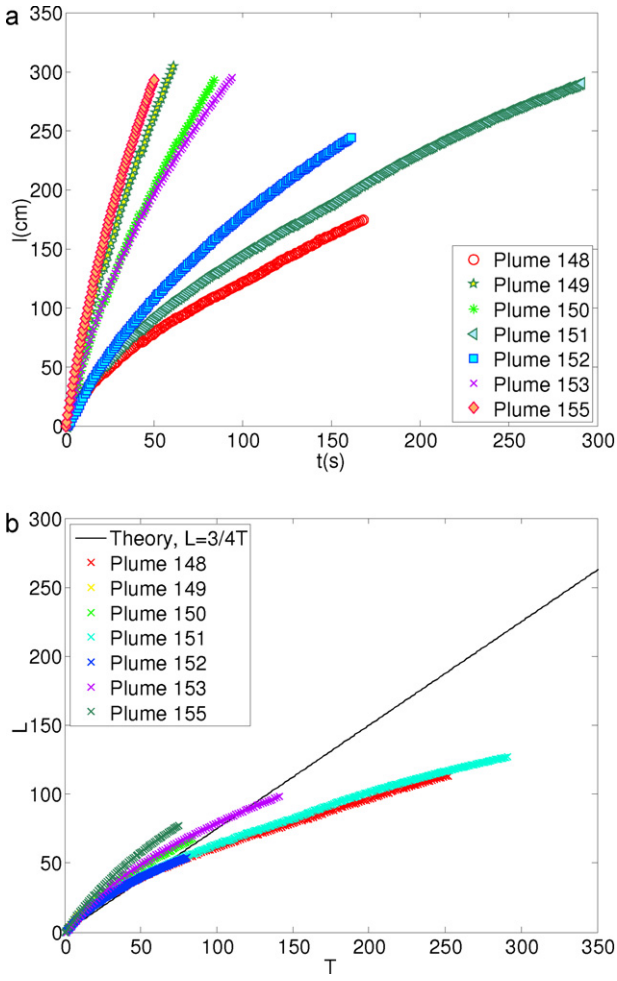

Fig. 8. Nose propagation of the viscous plumes. (a) Summary of the current length, l, as a function of time, t. (b) Summary of the non-dimensional current length, L, as a function of the non-dimensional time, T. The solid line represents the theoretical prediction, $L=(3/4)T$, of Thomas and Linden (2007).

To quantify the speed at which the inviscid plumes advance, we computed, for four of the ten numerical simulations, a single data fit of the form $L=a+bT$ for the dimensionless time, T, when the current flows at a nearly constant speed. The constant b in the fit is simply the current speed. The plumes reach a nearly steady velocity around $T=60$. Therefore we computed the fit for the four numerical simulations for which data exists for $T\geq 60$. From the values determined for a and b, we then calculated averages and associated standard deviations and found an averaged fit, $L=(21.32\pm 3.75)+(0.91\pm 0.12)T$. The value of the constant b, for the fit $L=a+bT$ in the *ROMS* inviscid numerical simulations, differs from the theoretical value of 3/4 by approximately +20%

From Figs. 8(b) and 9, the simulations with the lateral viscosity set to the molecular value no longer follow the geostrophic theory, but rather reproduce the results of the laboratory experiments. The discrepancies between the geostrophic model and the viscous numerical simulations (and therefore the laboratory experiments) are most significant when the lateral viscous forces are the greatest (that is for high values of the horizontal Ekman number, Ek_H).

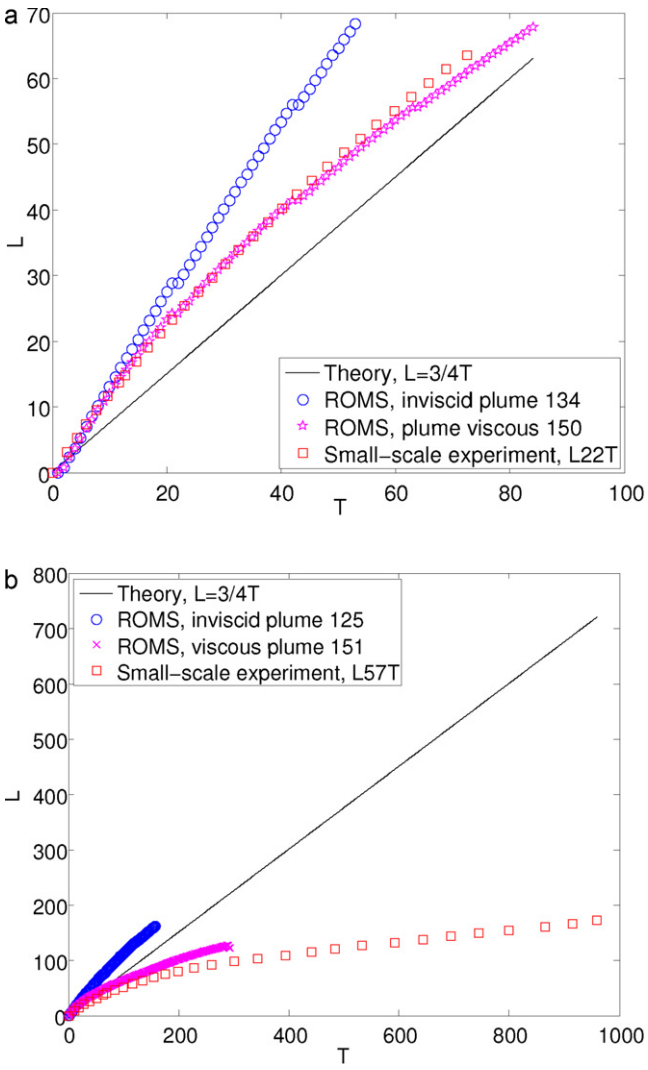

Fig. 9. Comparison of the non-dimensional current length, L, as a function of the non-dimensional time, T, for inviscid and viscous numerical simulations, and laboratory experiments of Thomas and Linden (2007). The solid line represents the theoretical prediction, $L = (3/4)T$. (a) $I = 0.3 \pm 0.033$, $Ek_V = (1.46 \pm 0.32) \times 10^{-3}$, L22T and plume 150: $Ek_H = (2.73 \pm 0.06) \times 10^{-4}$, plume 134; $Ek_H = 0$. (b) $I = 0.542 \pm 0.057$, $Ek_V = (1.26 \pm 0.03) \times 10^{-3}$, L57 and plume 151: $Ek_H = (1.16 \pm 0.2) \times 10^{-3}$, plume 125: $Ek_H = 0$.

3.3. Current width

Fig. 10(a) and (b) display the non-dimensional current width, W, as a function of the dimensionless time, T, measured at the non-dimensional distance, D_S, from the source, with $D_S = 12$, for all the inviscid and viscous numerical simulations, respectively. Data are non-dimensionalized by w_0. For some numerical simulations, width measurements were stopped before the end of the experiments due to the presence of instabilities in the currents.

In all the numerical simulations, the current widths continue to increase and do not approach a steady value over the duration of each simulation. From Fig. 10, the non-dimensional width measure-

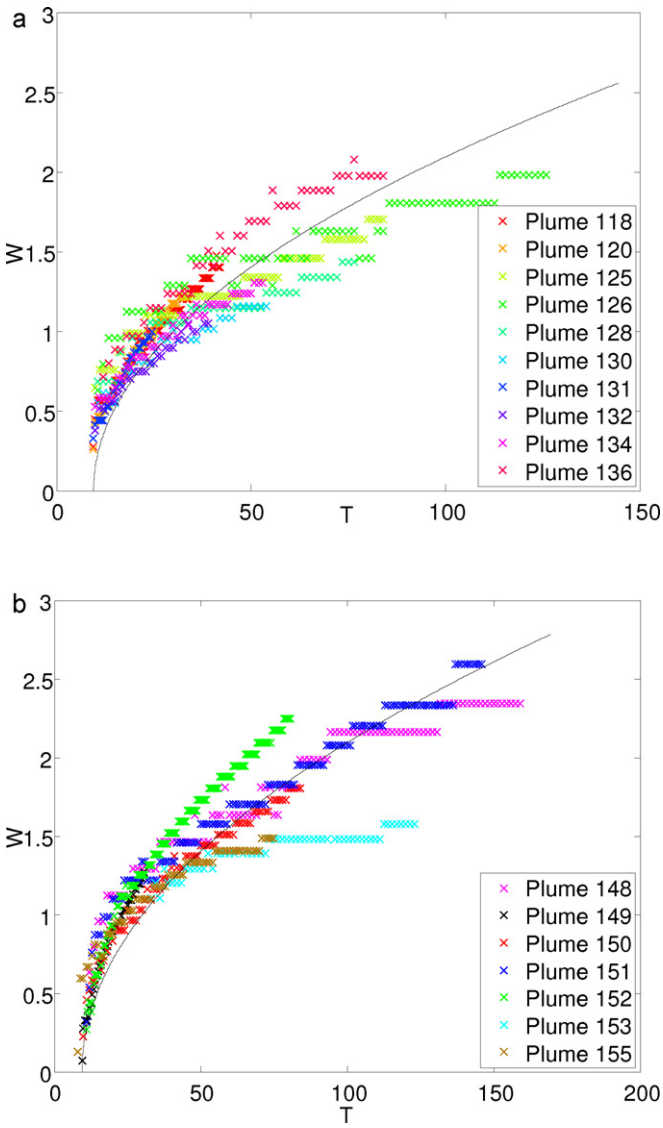

Fig. 10. Summary of the non-dimensional current width, W, as a function of the dimensionless time, T, for (a) all the inviscid numerical simulations and (b) all the viscous numerical simulations. The width was measured at the non-dimensional distance, D_S, from the source, with $D_S = 12$. The black curve on the figures of equation $0.22(T)^{1/2}$ is just to show that current widths grow as $T^{1/2}$.

ments closely cluster around a single curve, growing as $t^{1/2}$ (as was also found by Lentz and Helfrich (2002) and Thomas and Linden (2007)).

Of the ten inviscid numerical simulations and of the seven viscous numerical simulations, only seven inviscid numerical simulations and four viscous numerical simulations could be compared to the *PIV* experiments as one inviscid and one viscous simulation had no available laboratory experiment comparable to it, and two other inviscid and two other viscous numerical simulations had a laboratory experiment comparable to them which was unstable so that width measurements were

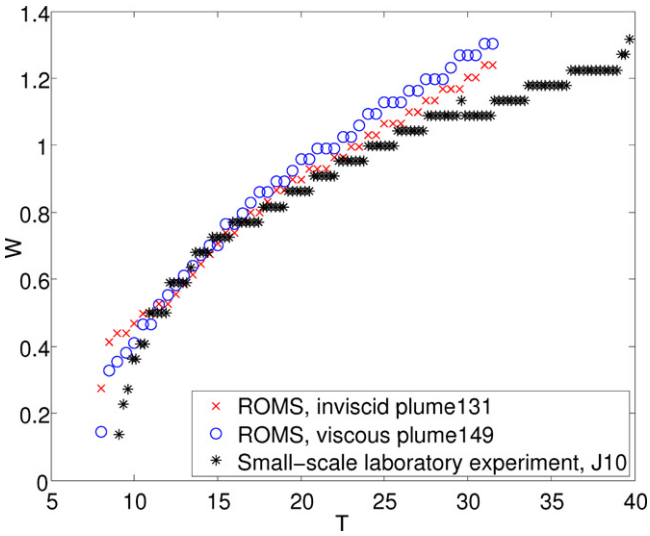

Fig. 11. Comparison of the non-dimensional current width, W, as a function of the dimensionless time, T, between one inviscid numerical simulation, one viscous numerical simulation and one laboratory experiments. The width was measured at the non-dimensional distance, D_S, from the source, with $D_S = 10$. $I = 0.126 \pm 0.03$, $Ek_V = (5.73 \pm 1.79) \times 10^{-3}$, inviscid simulation: $Ek_H = 0$, viscous simulation and laboratory experiment: $Ek_H = (1.26 \pm 0.29) \times 10^{-4}$.

not possible. The remaining seven inviscid numerical simulations and four viscous simulations are among the numerical simulations with the lowest values for the horizontal Ekman number, Ek_H.

Fig. 11 shows the non-dimensional current width, W, as a function of the dimensionless time, T, measured at the non-dimensional distance, D_S, from the source, with $D_S = 10$, for one of these seven inviscid simulations, for one of these four viscous simulations, and for one PIV laboratory experiment. The non-dimensionalizing factor of Ω for the time was different in some of the compared cases, thus leading to different non-dimensional curve lengths for the width. The overall agreement between the inviscid and viscous simulations and the laboratory experiments is found to be quite good. A comparison between the non-dimensional widths for the inviscid and viscous numerical simulations reveals that adding lateral viscosity does not change the width for the currents with low horizontal Ekman number, Ek_H.

3.4. Current velocity

In order to compare the theoretical geostrophic velocity to the inviscid and viscous numerical simulations, we look at the ratio, $U_{\max} = u_{\max}/u_0$, of the numerical/experimental maximum surface velocity, $u_{\max}$, to the theoretical velocity, u_0. The maximum surface velocity, $u_{\max}$, is measured at a fixed azimuthal position, for each time step. Thus at early time, the maximum surface velocity is extracted from the current nose and at later time, it is extracted from the coastal plume. The measurement position is far enough from the source so by the time the plume crosses it, the plume is supposed in geostrophic equilibrium.

Fig. 12 displays the maximum non-dimensional current speed, $U_{\max}$, as a function of the dimensionless time, T, measured at the dimensionless distance, D_S, downstream from the source, with $D_S = 10$, for one inviscid and one viscous simulation, and for one PIV laboratory experiment. The measurements were taken at the freshwater surface for the laboratory experiment and the viscous simulation, and at the freshwater surface ($N = 60$) and around 9 mm below the freshwater surface ($N = 60$) for the inviscid simulation.

From Fig. 12, one can see that the maximum value for $U_{\max}$ is in the front of the coastal current for the inviscid and viscous numerical simulations. Then it decreases until it reaches a nearly constant value (at $T = 15$, in Fig. 12), located inside the coastal current, behind the current head.

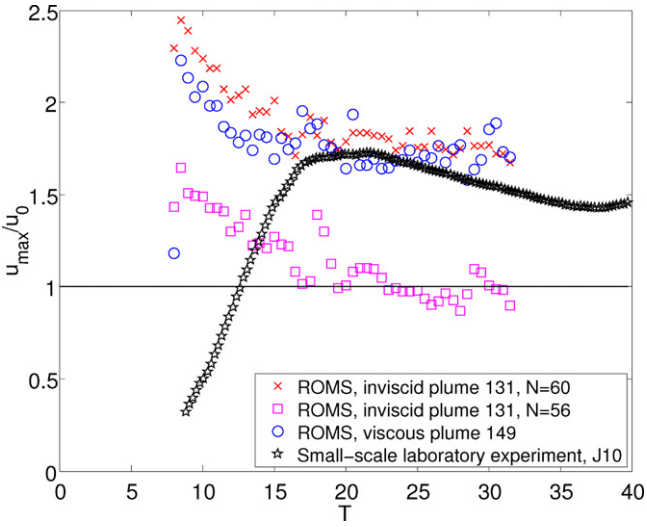

Fig. 12. Maximum non-dimensional current speed, U_{max}, as a function of the dimensionless time, T, measured at the non-dimensional distance, D_S, from the source, with $D_S = 10$, for one inviscid simulation, one viscous simulation and one laboratory experiment. U_{max} was measured at the surface for the laboratory experiment and the viscous simulation, and, at the surface ($N = 60$) and around 9 mm below the surface ($N = 56$) for the inviscid simulation. $I = 0.126 \pm 0.03$, $Ek_V = (5.73 \pm 1.79) \times 10^{-3}$, inviscid simulation: $Ek_H = 0$, viscous simulation and laboratory experiment: $Ek_H = (1.26 \pm 0.79) \times 10^{-4}$.

For currents with lower values for the horizontal Ekman number (e.g., plume 149 in Fig. 12), adding lateral viscosity in the simulations does not significantly influence the value of the maximum velocity, U_{max}, as T evolves. For currents with higher values for the horizontal Ekman number, adding lateral viscosity changes the value of the maximum velocity considerably as T evolves: currents with lateral viscosity have values for U_{max} much lower than the inviscid currents.

For the currents with lowest values for the horizontal Ekman number, the maximum velocity is larger than the theoretical prediction at the surface (Fig. 12). We investigated the value of the maximum velocity at different vertical levels, and we found that the geostrophic velocity, u_0, is approached inside the current, just below the water surface (around 9 mm below the freshwater surface as shown in Fig. 12). Thus the value of the maximum velocity of the currents from the simulations with lowest horizontal Ekman number lies near the value of the theoretically predicted geostrophic velocity, just below the freshwater surface, inside the coastal current.

Nine of the ten inviscid numerical simulations and six of the seven viscous numerical simulations could be compared to the *PIV* laboratory experiments. In contrast to the numerical results, the minimum value of U_{max} for the laboratory experiments is found in the front of the coastal current (Fig. 12). Then, it increases until it reaches its maximum value, located behind the nose, inside the coastal current; and there U_{max} attains a nearly constant value, similar to that in the numerical simulations. For currents with the lowest values of the horizontal Ekman number, reasonably good agreement for the maximum velocity is found between the inviscid and viscous simulations, and the laboratory experiments, inside the coastal current.

As we find relatively good agreement between laboratory experiments and numerical simulations for the maximum current velocity inside the coastal current, we might expect from the prior discussion that the maximum velocity from the laboratory experiments will also approach the geostrophic velocity just below the water surface. It is interesting to see that the geostrophic equilibrium is reached at the same non-dimensional time in the current for the inviscid and viscous simulations, and for the corresponding laboratory experiment (Fig. 12).

Two caveats are warranted. Less good agreement is found between the inviscid numerical simulations and the laboratory experiments with the highest values of Ek_H. Also, when the plumes in the laboratory and in the numerical simulations are unstable, the maximum velocity does not keep a

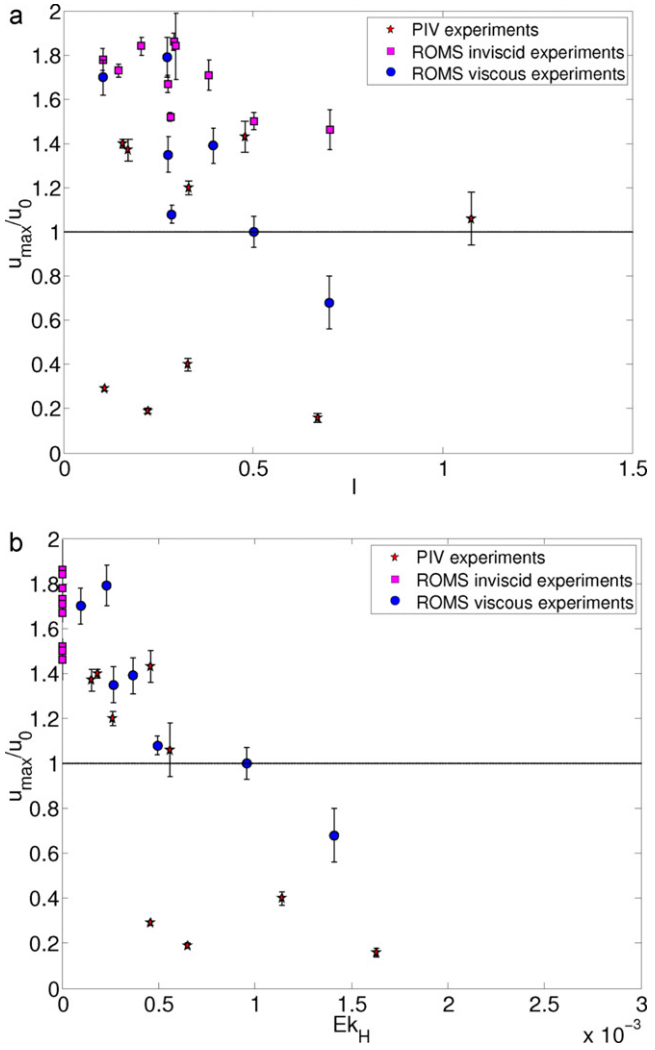

Fig. 13. Summary of the (averaged) maximum non-dimensional current speed, U_{max}, as a function of (a) the dimensionless parameter, I, and (b) the horizontal Ekman number, Ek_H, respectively, for the viscous and inviscid numerical simulations, and for the *PIV* laboratory experiments. The black line on the figures identifies $U_{max} = 1$, that is agreement between experiment and theory. The error bars are standard deviation errors of the averaged maximum non-dimensional current speed.

constant value inside the coastal plume. Instead, the maximum velocity is seen to fluctuate due to the presence of the instabilities.

Fig. 13(a) and (b) display a summary of the values for the non-dimensional current speed, U_{max}, as a function of the dimensionless parameter, I, and the horizontal Ekman number, Ek_H, respectively, for the inviscid and viscous *ROMS* simulations, and for the *PIV* laboratory experiments. The black line on the figures identifies $U_{max} = 1$, i.e. agreement between experiments and theory. To quantify the maximum non-dimensional current speed, U_{max}, in Fig. 13(a) and (b), U_{max} was averaged for each experiment from the non-dimensional time for which U_{max} is nearly constant. (In Fig. 12, U_{max} for the current from the laboratory experiment was averaged from $T = 25$, while U_{max} for the currents from the inviscid and viscous numerical simulations was averaged from $T = 16$.) The standard deviation was calculated for each value found for U_{max}. The maximum averaged non-dimensional current speed

could not be calculated for only one *PIV* experiment as fluctuations for $U_{\max}$ were too important due the presence of large instabilities in the gravity current.

Fig. 13(a) and (b) suggest an underlying dependence on the parameters I and Ek_H, although the dependence on Ek_H is tighter and scatter in the PIV experiments is great in both cases. From the *PIV* laboratory experiments and most clearly from the viscous numerical simulations displayed in Fig. 13(a), the value of $U_{\max}$ decreases as I increases[5].

From Fig. 13(b), it is clear that $U_{\max}$ decreases as Ek_H increases. For high values of the horizontal Ekman number„ simulated currents are slower than the theoretical prediction. Best agreement between experiments and theory is found for $Ek_H < 10^{-3}$, that is when the viscous forces are the smallest in the fluid system. Fig. 13(b) confirms the results obtained in Section 3.2.

3.5. Plume-edge instabilities

As mentioned in Section 3.1, instabilities along the outer plume edge were seen to develop in some of the numerical and laboratory experiments.

Fig. 14 shows the surface density field taken at the non-dimensional time $T = 168$ for the unstable plumes 148 and 151 from the viscous numerical simulations. We can see well-developed instabilities along the plume edge. One can see from Fig. 14 the rapid mixing of fresh and ambient waters within the growing instabilities.

Fig. 15 displays an I–Ek_H diagram summarizing the stability properties of the plumes simulated in the inviscid and viscous numerical simulations, and in the *PIV* laboratory experiments. The formation of instabilities is shown to depend on the magnitude of the parameters I and Ek_H. In particular, for finite values of Ek_H plumes with an I value greater than approximately 0.3 are unstable. Interestingly, the range of instability for the lowest values of Ek_H (e.g., the inviscid ROMS simulations) is somewhat reduced, with instabilities appearing for values of I greater than approximately 0.6.

The dimensionless parameter I is the ratio of the theoretical current height to the theoretical current width; it therefore characterizes the isopycnal slope. Large values of I imply currents that are deep and narrow. Currents with high values of I will have potential energy available to be released into the growing disturbances observed in the experiments. This suggests that the instabilities observed for experiments with high values of I are predominantly baroclinic, as the energy source for baroclinic instabilities is the potential energy in the fluid system.

From Griffiths and Linden (1981b), unstable disturbances are expected to be baroclinic for $\theta \gg 1$ and $\delta > 0.1$, where θ is the square of the ratio of the internal Rossby radius of deformation to the horizontal length scale of the flow, and δ is the fraction of the total fluid depth occupied by the layer inside the front. Here, the internal Rossby radius of deformation, R, is equal to $\sqrt{2}w_0$, where w_0 is the theoretical current width of Thomas and Linden (2007). Our experimental observations reveal that the measured width of the unstable coastal currents from the laboratory and numerical simulations were larger than w_0 and R, giving $\theta > 1$. Furthermore, by inspecting the ratio of the current depth to the total fluid depth for all numerical and laboratory unstable experiments, we found that this ratio is always greater than 0.1.

4. Departures from the theory: internal structure and dynamics

The geostrophic theory of Thomas and Linden (2007) assumes that the buoyant current is steady, x-invariant and inviscid. It further requires the current velocity to vanish at the coast, and to achieve its maximum strength where the density front intersects the surface. Although the bulk properties of the plumes observed in the laboratory and simulated in ROMS are in generally good agreement with the theoretical predictions, some departures from the theory are nonetheless evident. We explore some of these next.

[5] A figure similar to Fig. 13(a) can be constructed from the experiments of Thomas and Linden (2007) (see their Fig. 9) for the experimental mean velocity, u_{mean}. Experimental mean current speed is found to be slower than the theoretical prediction for the largest values of I (that is for the deepest and the narrowest currents).

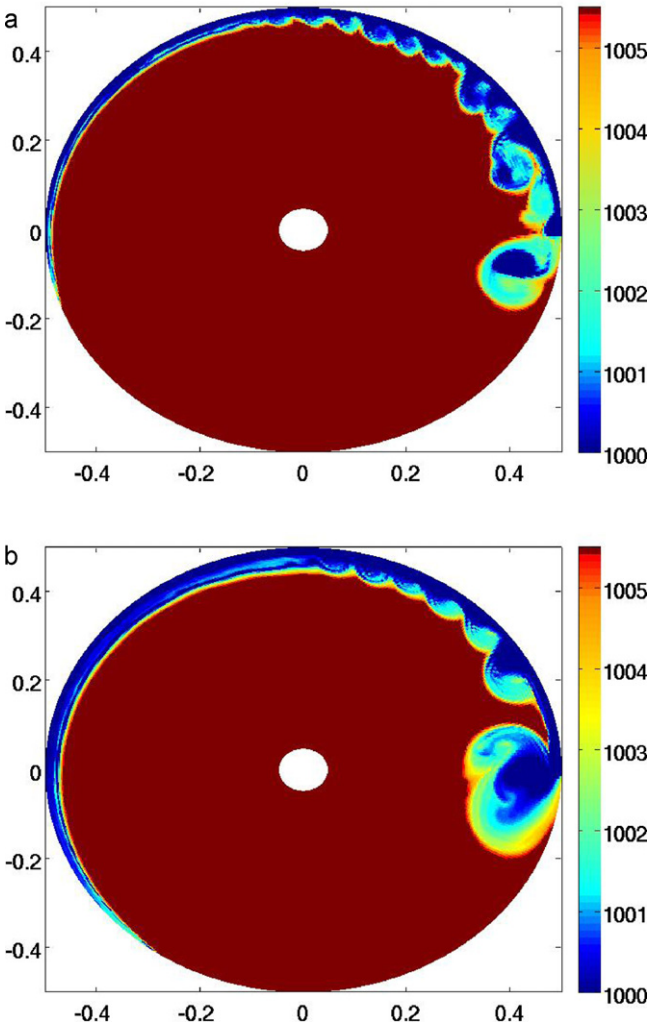

Fig. 14. Surface density field showing the unstable plumes (a) 148 and (b) 151 from the viscous numerical simulations. Color bar is for density (in kg m^{-3}).

4.1. Internal velocity structure and momentum balances

The geostrophic theory is clearly not meant to represent the early evolution of the bulge and developing plume. Therefore it is perhaps not surprising that the early-time properties of the plume differ from the theoretical predictions. One obvious departure from the theory early on is the observed magnitude of fluid velocity in the plumes. The fluid speeds are initially much greater than the geostrophic estimates in the numerical simulations. By contrast, they are much slower initially in the PIV laboratory experiments.

One explanation for these departures might be that the early plumes are ageostrophic to a significant degree, approaching a state of geostrophic balance only later in time. One advantage of the *ROMS* numerical simulations is that the internal structure of the plumes and the accompanying dynamical balances may be readily investigated. Fig. 16(a)–(d) display cross-sections in the y–z plane of the time-averaged density field, the time-averaged non-dimensional along-shore velocity, U, the time-averaged

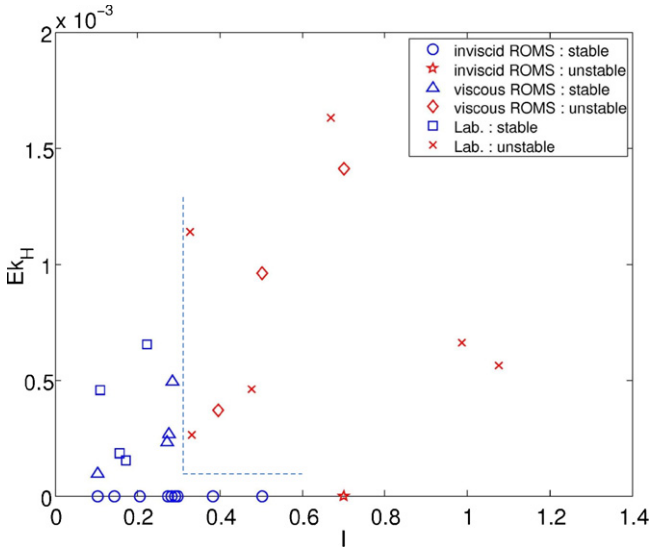

Fig. 15. I–Ek_H diagram displaying the parametric locations where the plumes are found to be stable/unstable. The dashed line is suggestive of the stability boundary.

non-dimensional Coriolis term in the v-momentum equation, and the time-averaged non-dimensional pressure gradient term in the v-momentum equation, respectively, taken at the non-dimensional distance downstream from the source, $D_S = 3.69$, and at the non-dimensional time, $T = 4.25$, for the viscous plume 150. The along-shore velocity in Fig. 16b is non-dimensionalized by the theoretical geostrophic velocity, u_0, and the Coriolis and pressure gradient terms in Fig. 16(c) and (d) are non-dimensionalized by (fu_0) where f is the Coriolis parameter. The time average in each case has been taken over 0.5 non-dimensional time units (0.5 s).

The initial structure of the density field within the developing plume (Fig. 16(a)) has a strong sloping front, as given by the theory, although the isopycnal slope is rather more linear than quadratic (as given by the theory). The accompanying along-shore flow (Fig. 16(b)) has its maximum at the surface and off-shore, roughly contiguous with the surface density front; this is also in agreement with the theory, which predicts a linear offshore increase. The velocity decreases towards the annular wall; however, it does not in general vanish at the wall, as required by the theory.

At $T = 4.25$, the flow is already nearly geostrophic; the Coriolis and pressure gradient terms in the cross-shore momentum equation nearly balance (Fig. 16(c) and (d)). The next largest terms are those making up the total time rate of change (local acceleration and advection; not shown), but these are much smaller and have no clear spatial pattern. Lastly, explicit viscous forces (plume 150 is viscous) are smaller by one to two orders of magnitude; they apparently play little role in the early plume development. In support of this conclusion, plume 134 (the inviscid companion to 150) is found to have nearly identical cross-plume structure early on.

In agreement with the results presented in section 3, the maximum current speed in the early plume exceeds the theoretical estimate by a factor of about two. Since the early plume is nearly geostrophic, the pressure gradient force must also exceed that suggested by theory (Fig. 16(d)). Note that the early speeds in the PIV laboratory experiments were decidedly slower than those in the theory. If the early development in the laboratory plumes is also nearly geostrophic, as is likely, then we can conclude that the pressure gradients present in the laboratory setting were much weaker than in the theory. These differences in early current speeds are presumably attributable to differences in the buoyancy injection mechanisms employed in the laboratory experiments and numerical simulations, this being the only significant difference between the two implementations.

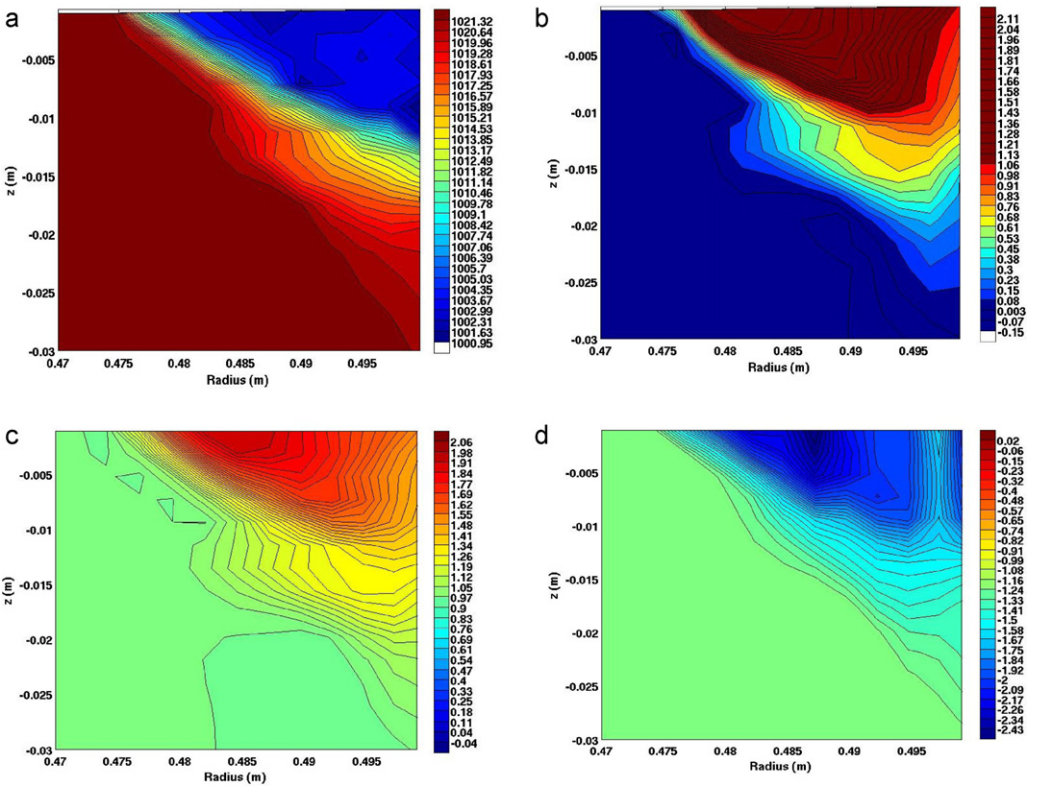

Fig. 16. Cross-section in the y–z plane of (a) the density field, (b) the non-dimensional along-shore velocity, U, (c) the non-dimensional Coriolis term in the v-momentum equation, and (d) the non-dimensional Pressure Gradient term, taken at the non-dimensional distance downstream from the source, $D_S = 3.69$, and at the non-dimensional time, $T = 4.25$, for the viscous plume 150.

However, without more detailed dynamical information from the laboratory this hypothesis cannot be confirmed.

We have already remarked that growing departures from the geostrophic theory are observed for elevated values of the horizontal Ekman number. Therefore, the influences of horizontal viscosity must eventually become consequential at later times in the propagation of the plumes. Fig. 17(a)–(d) display cross-sections in the y–z plane of the time-averaged density field, and time-averaged non-dimensional along-shore velocity, U, respectively, taken at the non-dimensional distance upstream from the nose, $D_N = 2.32$, and at the non-dimensional time, $T = 36.25$, for the inviscid plume 134 and the viscous plume 150. The along-shore velocity in Fig. 17(c) and (d) has been non-dimensionalized by the theoretical geostrophic velocity, u_0. (The non-dimensional distance along the annulus corresponds roughly to the point opposite to the source of buoyancy.) For comparison, Fig. 18(a) and (b) display the cross-section in the (x)–(z) plane of the density field taken at 4.8 mm from the wall at the non-dimensional time $T = 53$, for the inviscid plume 134 and the viscous plume 150.

Inspection of Figs. 17(a)–(d) and 18(a), (b) indicates that the frontal structure accompanying the viscous plume 150 is both wider and deeper than that in its inviscid counterpart, plume 134. At this later time, the accompanying current jet is stronger in the inviscid experiment. The azimuthal profile of the current depth displayed in Fig. 18(a) and (b) reveals that current depth decreases along the wall but only in the final plume length, contradicting Thomas and Linden (2007) who suggested that currents decreased in depth linearly along the coastal wall.

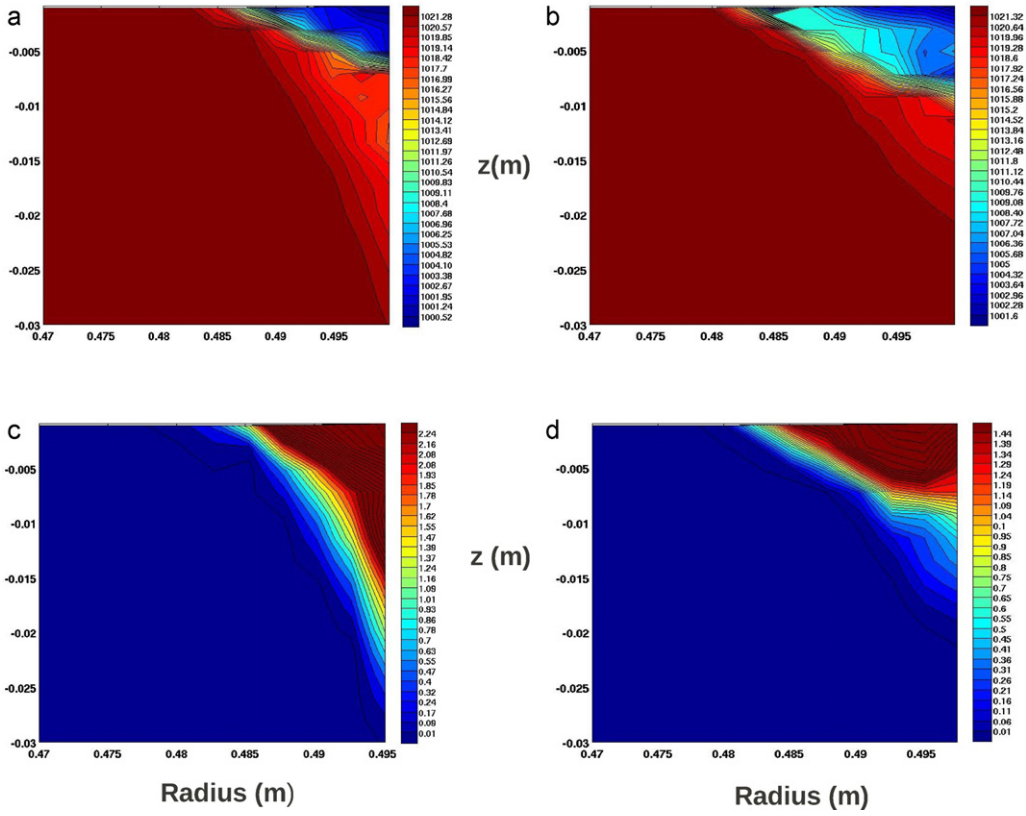

Fig. 17. Cross-section in the y–z plane of (a)–(b) the density field for the inviscid plume 134 and the viscous plume 150, respectively, and (c)–(d) the non-dimensional along-shore velocity, U, for the inviscid plume 134 and the viscous plume 150, respectively, taken at the non-dimensional distance upstream from the nose, $D_N = 2.32$, and at the non-dimensional time, $T = 36.25$. The color bar in the top images is for density (in kg m^{-3}).

4.2. Mixing in the plumes

Dissipation and mixing occur in the laboratory and numerical experiments in several different ways. (Of course, mixing is disregarded in the geostrophic theory.) In the numerical simulations, mixing of momentum and density occurs in at least three distinct ways, each of which has its own efficiency and consequence. The first way is by explicit viscosity and diffusivity (though the latter has been set to zero in all these *ROMS* simulations). Viscous forces, if present, lead to a net loss of momentum from the plume via stresses that develop at the annulus wall. The accompanying viscous sidewall boundary layer arising from explicit viscosity in *ROMS* is narrow (in fact, contained within a single numerical grid point). However its influence is conveyed to the interior fluid by advection and other types of mixing.

A second contribution to mixing in the numerical simulations is via resolved sub-plume-scale instabilities (Section 3.5). This internal mixing via resolved, albeit small-scale, processes is conservative (i.e., does not lead to a net gain or loss of momentum or density). Finally, mixing will arise from implicit smoothing associated with the finite difference implementation of (especially) horizontal advection. This leads to internal smoothing but also has no non-conservative consequences (if the model is properly designed and coded!).

Mixing in the laboratory experiments arises from both molecular viscous and diffusive action, and turbulent mixing associated with (e.g.) plume-edge instabilities. There is no direct analogue of the

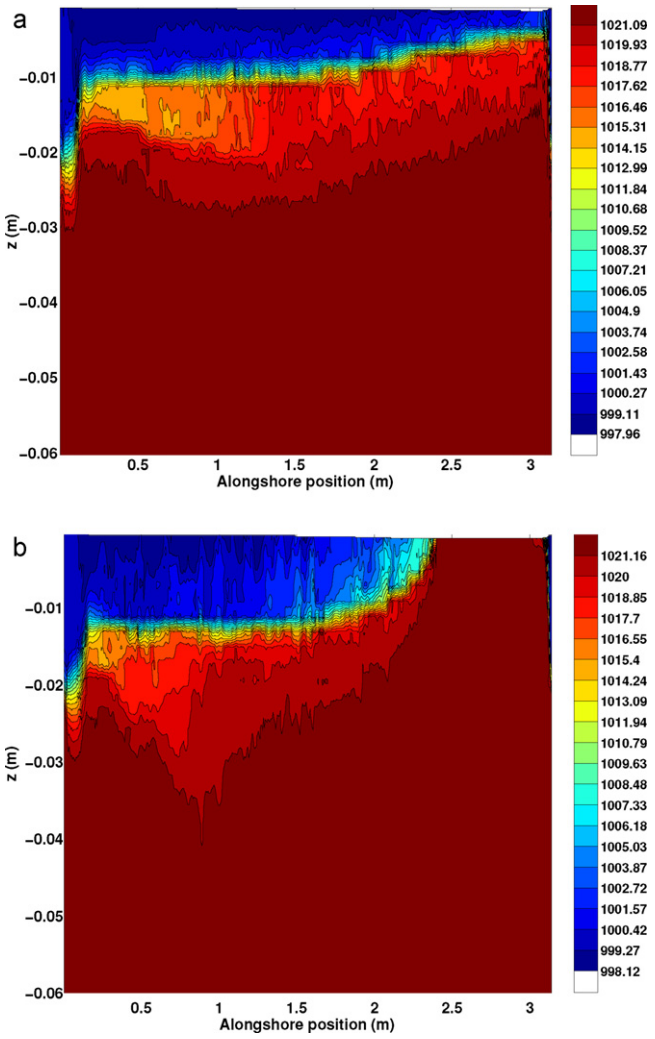

Fig. 18. Cross-section in the (x)–(z) plane of the density field taken at 4.8 mm from the wall at the non-dimensional time $T = 53$, for the inviscid plume 134 and the viscous plume 150.

discretization-associated smoothing as in *ROMS*. Therefore it is relevant to inquire as to the potential impact of implicit smoothing in the numerical simulations.

Advection of momentum in these ROMS simulations is accomplished using a third-order upwind algorithm (Haidvogel et al., 2007) and the advection of tracers (i.e., density) using the multidimensional positive definite advection transport algorithm (MPDATA; Smolarkiewicz and Szmelter, 2005). The implicit smoothing associated with the *ROMS* third-order upwind advection scheme is of biharmonic form with a hyper-viscosity coefficient proportional to the third power of the horizontal grid spacing and to the first power of the current speed. The resulting smoothing is very scale-selective, and is essentially negligible on any spatial scale above a few grid spaces. The positive-definite MPDATA algorithm used for density is less scale-selective in its smoothing, as it has been designed to (approximately) insure positivity of tracer fields. It is therefore likely that, in the absence of turbulent mixing by the plume-edge instabilities, the thickness of the density fronts in *ROMS* are being determined by

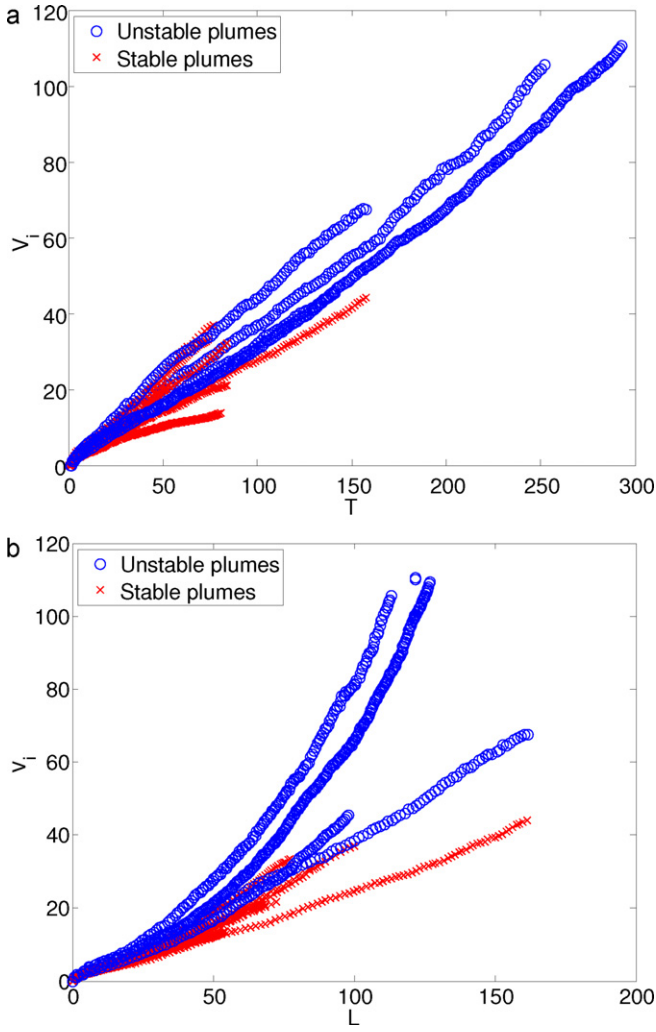

Fig. 19. Non-dimensional volume, V_i, of intermediate water in the coastal current and bulge system, as a function of (a) the dimensionless time, T, and (b) the non-dimensional current length, L, for the inviscid and viscous numerical simulations.

the tracer advection algorithm. As the frontal structure of the plume is being well maintained in these simulations (Fig. 17(a)–(d)), the tracer advection scheme is not overly diffusive.

It is interesting to inquire whether we can quantify the mixing associated with the plume-edge instabilities in the numerical simulations. One way to approach this is to measure, as a function of time, the rate of production of intermediate water, that is, water with a value of density intermediate between that of the ambient and buoyant fluids. As viscous effects are confined to the wall boundary layer (and explicit diffusivity is omitted), mixing of density in the numerical plumes arises solely from two sources: implicit smoothing due to discretization, and the mixing associated with the plume-edge instabilities, should the latter arise.

Fig. 19(a) and (b) display the non-dimensional volume of intermediate water in the gravity current and bulge system as a function of the dimensionless time, T, and the non-dimensional current length, L, extracted from Figs. 7(b) and 8(b), for the inviscid and viscous simulations. The volume of intermediate water in Fig. 19 is non-dimensionalized by $(q_0/\Omega 2)$. The range of the density values for the intermediate

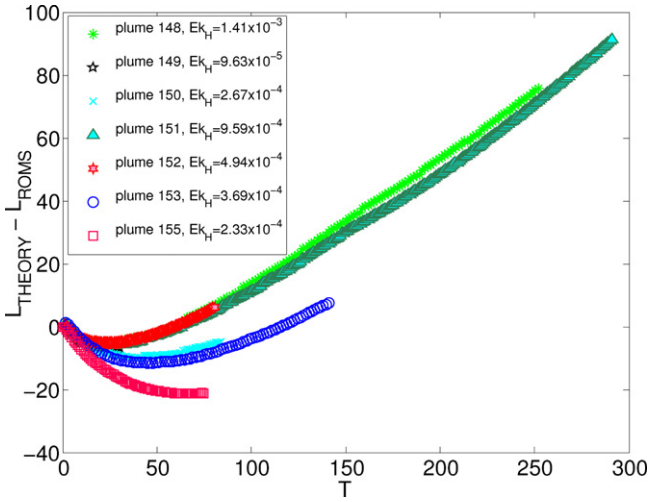

Fig. 20. Difference between the non-dimensional current length, L, for the viscous numerical simulations and the theory of Thomas and Linden (2007), $L = (3/4)T$.

water in each experiment was chosen to extend from $(1000 + 0.46 \times \Delta(\rho))$ to $(1000 + 0.82 \times \Delta(\rho))$, thereby occupying 36% of the total range of the density in the experiment.

Fig. 19(a) and (b) shows that the non-dimensional rates at which intermediate water is formed have some interesting, and perhaps non-intuitive, dependencies. Fig. 19(a), in which the rate of mixing is plotted against non-dimensional time (T), suggests a time rate of mixing that is rather similar across all numerical simulations. In particular, the range of values for these *rates* do not appear to depend importantly on whether the plumes are stable or unstable. Despite this, Fig. 19(a) does make clear that the *total amount of mixing* undergone in a single experiment is much greater for the unstable experiments. The explanation is, of course, that the viscous plumes are advancing more slowly and therefore take more time to complete a circuit about the annulus.

If one plots the volume of intermediate water against *distance traveled* (Fig. 19(b)), a different picture emerges. The unstable plumes are clearly more effective at mixing *per unit distance traveled*. We recall from Section 3.5 that the addition of viscosity increased the region in I parameter space in which instabilities were observed to occur. The addition of viscosity also acts to decelerate the plumes. The observation that total mixing is enhanced within the slow-moving plumes therefore appears to be at least consistent with the results presented above. However, whether the enhanced region of instability accompanying the addition of viscosity is due to the physics or the numerics (or both) is not immediately obvious.

4.3. The role of viscosity

As the foregoing sections illustrate, the assumptions underlying the geostrophic theory of Thomas and Linden (2007) are only approximately met in the laboratory experiments and the numerical simulations. Perhaps the most obvious disagreement pertains to the role of lateral viscosity. Whereas the geostrophic theory envisions an inviscid ocean, both the laboratory and numerical results underscore the importance of lateral viscous forces. In particular, the speed of the buoyant plume is observed to depend on the magnitude of the viscous forces as measured by the horizontal Ekman number, Ek_H.

Fig. 20 shows the departure of the non-dimensional current length given by ROMS from that predicted by the geostrophic theory. As noted above, the initial displacement of the plume is faster than the theory would provide. However, the plumes eventually decelerate and reach a nearly constant speed that is less than the theoretical value. This suggests that viscosity is providing a decelerating force that partially offsets the geostrophic pressure gradient supporting the geostrophic flow.

We examine the potential role of the viscous forces employing a slight modification of the theory proposed by Thomas and Linden (2007). Retaining many of their original assumptions – i.e., x-invariant, rotationally dominated, steady flow – we introduce molecular viscous forces in the cross-plume direction, and allow a non-zero transverse velocity component (v). The equations that result are:

$$fv = \nu \frac{\partial^2 u}{\partial y^2}, \tag{7}$$

$$fu = -\left(\frac{1}{\rho}\right)\frac{\partial p}{\partial y} + \nu \frac{\partial^2 v}{\partial y^2}. \tag{8}$$

These are the familiar equations for an Ekman layer (although here the layer is a sidewall layer as opposed to a boundary layer at the ocean surface).

We therefore proceed as usual and imagine that, in the interior of the plume, a geostrophic balance is preserved, and that the action of viscosity occurs primarily in a narrow boundary layer adjacent to the coastal wall. The geostrophic velocity in the plume is in balance with the pressure gradient; that is,

$$fu_g = -\left(\frac{1}{\rho}\right)\frac{\partial p}{\partial y}. \tag{9}$$

The plume will be retarded by the viscous stress at the wall. With no-slip boundary conditions on the wall, it is easily shown that the viscous stress at $y = 0$ that arises due to the sidewall Ekman layer is given by:

$$\left(\nu \frac{\partial v}{\partial y}\right)|_{y=0} = \left(\frac{fv}{2}\right)^{1/2} u_g. \tag{10}$$

Assuming the viscous stress to vanish outside the sidewall boundary layer, the viscous forces in Eq. (8) can be estimated as

$$\nu \frac{\partial^2 v}{\partial y^2} = \frac{(fv2)^{1/2} u_g}{\alpha w_0} \tag{11}$$

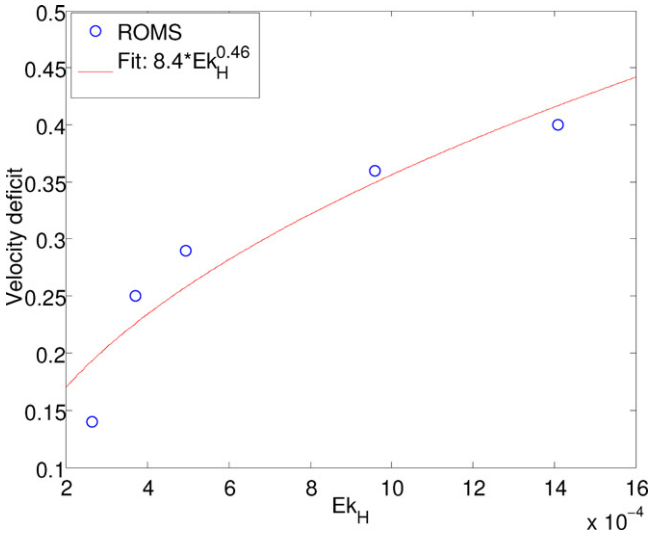

Fig. 21. Velocity deficit as a function of the horizontal Ekman number, Ek_H. The curve is the best fit for the data of the form $a \times (Ek_H)^b$ where a and b are constants. The velocity deficits are simply the slope of the best linear fits for the curves of Fig. 20 computed from the time, T_E, when equilibrium is reached in the system.

where we have assumed a boundary layer width αw_0 where α is imagined to be a small constant. Rearranging, we get:

$$u = u_g \left(1 - \left(\frac{1}{2}\right)^{1/2} \left(\frac{1}{\alpha}\right) (Ek_H)^{1/2}\right). \tag{12}$$

In this simple view, the velocity discrepancy is therefore seen to be proportional to the square root of the horizontal Ekman number.

We can assess this simple argument using the curves in Fig. 20. Linear fits are produced to the curves in Fig. 20 for $T \geq 50$. The slopes given by these fits represent estimates of the velocity discrepancy for each of the simulations. Fig. 21 shows the resulting estimates of velocity discrepancy plotted against the horizontal Ekman number. An approximate dependence on the horizontal Ekman number to the one-half power is indeed observed to hold. The implied value of α is approximately 1/12, suggesting an inner boundary layer width comparable to the numerical grid spacing.

5. Summary and conclusion

Numerical simulations, conducted with the Regional Ocean Modeling System (*ROMS*), and investigating the dynamics of gravity-driven coastal currents, have been described. Two complementary studies have been performed: one without explicit lateral viscosity (inviscid) and another using the molecular value of viscosity. The purposes of the investigation are two-fold: first, to quantify departures from the geostrophic theory of Thomas and Linden (2007), and second, to investigate the internal dynamics of the developing plumes.

The model of Thomas and Linden (2007) assumes steady inviscid currents, invariance in the along-shore direction, geostrophic equilibrium, and a dominant along-shore velocity which vanishes at the coast. To assess these assumptions, results from the numerical studies were compared to the geostrophic model of Thomas and Linden (2007), to their small-scale laboratory experiments, and to a complementary set of laboratory experiments conducted at Warwick University (the latter using the *PIV* method to better identify current widths and surface velocity fields). The kinematic properties (lengths, widths, velocities) of the experimental and numerical currents were determined and compared. Dependences on the primary non-dimensional parameters – the non-dimensional isopycnal slope, I, and the horizontal Ekman number, Ek_H – were also determined.

Upon release of the buoyant water in the numerical and laboratory experiments, both an anti-cyclonic bulge growing in the vicinity of the estuary and a coastal current flowing downstream of the bulge in the direction of Kelvin wave propagation are found to develop. The rate of elongation of the plumes in the inviscid numerical simulations typically exceeds the estimate given by the geostrophic theory, and approaches the best rate of elongation of the plumes produced in the laboratory experiments conducted at smallest horizontal Ekman number. In contrast, the rate of elongation of the plumes in the viscous numerical simulations duplicates quite well the rate of the elongation of the plumes in the laboratory experiments at comparable horizontal Ekman number.

During the initial evolution of the plumes from the viscous numerical simulations, the plume propagation rate was larger than the geostrophic prediction, then the plumes decelerated to finally propagate at nearly constant speed. The magnitude of the plume deceleration was most important at the highest values of the horizontal Ekman number. The discrepancies between the viscous numerical simulations (and thus laboratory experiments) and the geostrophic model for the plume propagation rate were the most significant when the lateral viscous forces were the largest (that is, for high horizontal Ekman number). The dimensionless number, I (characterizing the isopycnal slope) was also noticed to have an impact on current propagation speed: plumes with a large isopycnal slope (large I), that is plumes which are deep and narrow, were observed to be slower than the predicted geostrophic velocity.

Current widths increase over the duration of each experiment, and follow a simple curve growing as $t^{1/2}$. Agreement between numerical simulation and *PIV* experiments was found for currents with small horizontal Ekman number. Current width for the numerical simulations and laboratory experiments at large horizontal Ekman number could not be compared as instabilities occurred in these plumes

and made the width measurement unreliable. The current depth profile in the numerical simulations is observed to decrease along the wall only in the final portion of the plume length, contradicting Thomas and Linden (2007) who suggested a linear decrease for the current depth along the coastal wall.

Maximum surface velocities were measured and compared for the numerical simulations and *PIV* experiments at a fixed distance downstream from the source as a function of time. At early times, the maximum surface velocity was extracted from the current nose and at a later time, it was extracted from the coastal plume. In the nose region, the maximum surface velocities were the highest in the numerical simulations and exceeded the theoretical prediction by a factor of about 2. By contrast, in the laboratory experiments, the maximum surface velocities were the lowest in the nose and were much slower than the geostrophic velocity. These differences are suggested to have arisen from differences in the buoyancy injection mechanisms employed in the laboratory experiments and numerical simulations. Maximum surface velocities of the numerical simulations compared quite well with the maximum surface velocities of the *PIV* experiments at small horizontal Ekman number inside the coastal plume (not at the nose). From examination of the maximum velocity in the numerical simulations at different vertical levels, the geostrophic velocity given by theory is not reached at the surface but instead below the surface (around 1 cm below the freshwater surface).

The internal dynamics of the plumes were examined by producing cross-plume and along-plume momentum balances. The numerical plumes were found to rapidly attain geostrophic balance with a maximum velocity in the plume greater than the theoretically expected geostrophic velocity. This is in agreement with the observed maximum surface velocities in the PIV experiments.

Instabilities are observed to develop along the plume edge for some experimental parameter combinations. The formation of the instabilities observed in the present experiments depends on the magnitude of the horizontal Ekman number and the dimensionless parameter, I, characterizing the isopycnal slope. Values of I greater than 0.3 generally produce instabilities in the buoyant outflow. The instabilities are expected to be predominantly baroclinic as currents with large values of I are deep and narrow, and then have enough potential energy available to be released in the instability process. The rate of mixing in the buoyant plumes, estimated from the rate of production of water of intermediate density, did not appear to depend importantly on whether the plumes were stable or unstable. However, the total amount of mixing undergone in a single experiment was much greater for the unstable experiments. The two results are reconciled by noting that the viscous unstable experiments occupy a longer elapsed time.

Overall, the theory of Thomas and Linden (2007) is found to best reproduce the coastal currents with the weakest viscous forces, but substantial departures from the theory occur as viscous forces increase. An extension of the theory considering viscous forces suggests that the discrepancy between the geostrophic and the observed current speeds should be proportional to the square root of the horizontal Ekman number, Ek_H. This has been confirmed in the viscous simulation results.

The dependence on the magnitude of the horizontal Ekman number for the plume propagation speed is consistent with the scaling of the results of Thomas and Linden (2007) for the current width as a function of Reynolds number. The Reynolds number of Thomas and Linden (2007) is inversely proportional to the horizontal Ekman number presented in this study ($\mathrm{Re} = (3/8) \times (1/Ek_H)$). Thus their results for the current width can be interpreted as follows: for very large horizontal Ekman number (thus low Reynolds number), experimental currents are wider than the theoretical prediction, while for very low Ekman number (thus large Reynolds number) currents are thinner than the theoretical prediction. When combining their results with the results of the present study, we find that currents are wider and slower than theory when the viscous forces are the greatest, while currents are thinner and faster than the prediction when the viscous forces are the most negligible. Thus viscous forces affect speed and shape of coastal currents.

Additional laboratory experiments have now been conducted in an extension to the study of Thomas and Linden (2007) to investigate the effects of an inclined coastline topography. An extension of the geostrophic theory of Thomas and Linden (2007) has also been developed to predict the kinematic properties of currents flowing along an inclined coastline. Finally, the impact of viscosity on currents flowing along a bottom slope has been examined. Papers summarizing the results of these studies are in preparation.

Acknowledgements

The first author would like to thank Pr. Peter Thomas for his *PhD* supervision and Dr. Mark Brend for his helpful discussions. We are also grateful to the two anonymous reviewers for providing detailed comments that have greatly improved the content and clarity of this work.

References

Avicola, G., Huq, P., 2002. Scaling analysis for the interaction between a buoyant coastal current and the continental shelf: experiments and observations. J. Phys. Oceanogr. 32 (November (11)), 3233–3248.
Avicola, G., Huq, P., 2003a. The characteristics of the recirculating bulge region in coastal buoyant outflows. J. Mar. Res. 61 (4), 435–463.
Avicola, G., Huq, P., 2003b. The role of outflow geometry in the formation of the recirculating bulge region in coastal buoyant outflow. J. Mar. Res. 61 (4), 411–434.
Chabert D'Hières, G., Didelle, H., Obaton, D., 1991. A laboratory study of surface boundary currents: application to the algerian current. J. Geophys. Res. 96 (July (C7)), 12.539–12.548.
Chant, R.J., 2011. Interactions between estuaries and coasts: river plumes—their formation transport and dispersal. In: Wolanski, E., McLusky, D.S., Monismith, S., Uncles, R. (Eds.), Treatise on Estuarine and Coastal Science. Elsevier Press.
Chant, R.J., Glenn, S.M., Hunter, E., Kohut, J., Chen, R.F., Houghton, R.W., Bosch, J., Schofield, O., 2008. Bulge formation of a buoyant river outflow. J. Geophys. Res. 113, C01017.
Chao, S.-Y., Boicourt, W.C., 1986. Onset of estuarine plumes. J. Phys. Oceanogr. 16 (December), 2137–2149.
Chapman, D.C., Lentz, S.J., 1994. Trapping of a coastal density front by the bottom boundary layer. J. Phys. Oceanogr. 24 (July (7)), 1464–1479.
Csanady, G.T., 1984. Circlation induced by river inflow in well mixed water over a sloping continental shelf. J. Phys. Oceanogr. 14 (November (11)), 1703–1711.
Fong, D.A., Geyer, W.R., 2002. The alongshore transport of freshwater in a surface-trapped river plume. J. Phys. Oceanogr. 32 (March (3)), 957–972.
Garvine, R., 1995. A dynamical system for classifying buoyant coastal discharges. Cont. Shelf Res. 15, 1585–1596.
Griffiths, R.W., Hopfinger, E.J., 1983. Gravity currents moving along a lateral boundary in a rotating fluid. J. Fluid Mech. 134, 357–399.
Griffiths, R.W., Linden, P.F., 1981a. The stability of buoyancy-driven coastal currents. Dyn. Atmos. Oceans 5, 281–306.
Griffiths, R.W., Linden, P.F., 1981b. The stability of vortices in a rotating, stratified fluid. J. Fluid Mech. 105, 283–316.
Haidvogel, D.B., Arango, H., Budgell, W.P., Cornuelle, B.D., Curchitser, E., Lorenzo, E.D., Fennel, K., Geyer, W.R., Hermann, A.J., Lanerolle, L., Levin, J., McWilliams, J.C., Miller, A.J., Moore, A.M., Powell, T.M., Shchepetkin, A.F., Sherwood, C.R., Signell, R.P., Warner, J.C., Wilkin, J., 2007. Ocean forecasting in terrain-following coordinates: formulation and skill assessment of the regional ocean modeling system. J. Comput. Phys. 227, 3595–3624.
Hickey, B.M., Pietrafesa, L.J., Boicourt, W.C., 1998. The colombia river plume study: subtidal variability in the velocity and salinity fields. J. Geophys. Res. 103 (May (C5)), 10339–10368.
Horner-Devine, A.R., Fong, D.A., Monismith, S.G., Maxworthy, T., 2006. Laboratory experiments simulating a coastal river inflow. J. Fluid Mech. 555, 203–232.
Lentz, S.J., Helfrich, K.R., 2002. Buoyant gravity currents along a sloping bottom in a rotating fluid. J. Fluid Mech. 464, 251–278.
Liu, Y., MacCready, P., Hickey, B.M., Dever, E.P., Kosro, P.M., Banas, N.S., 2009. Evaluation of a coastal ocean circulation model for the columbia river plume in summer 2004. J. Geophys. Res., 114.
Munchow, A., Garvine, R.W., 1993a. Buoyancy and wind forcing of a coastal current. J. Mar. Res. 51, 293–322.
Munchow, A., Garvine, R.W., 1993b. Dynamical properties of a buoyancy-driven coastal current. J. Geophys. Res. 98 (November (C11)), 20063–20077.
Obaton, D., Millot, C., Chabert D'Hières, G., Taupier-Letage, I., 2000. The algerian current: comparison between in situ and laboratory data sets. Deep-Sea Res. Part I 47, 2159–2190.
Oey, L.Y., Mellor, G.L., 1993. Subtidal variability of estuarine outflow, plume, and coastal current: a model study. J. Phys. Oceanogr. 23 (January (1)), 164–171.
Rivas, D., Velasco Fuentes, O.U., Ochoa, J., 2005. Topographic effects on the dynamics of gravity currents in a rotating system. Dyn. Atmos. Oceans 39, 227–249.
Shchepetkin, A.F., McWilliams, J.C., 2005. The regional ocean modeling system (roms): a split-explicit, free-surface, topography-following coordinates ocean model. Ocean Model. 9, 347–404.
Smolarkiewicz, P.K., Szmelter, J., 2005. Mpdata: an edge-based unstructured-grid formulation. J. Comput. Phys., 206.
Thomas, P.J., Linden, P.F., 2007. Rotating gravity currents: small-scale and large-scale laboratory experiments and a geostrophic model. J. Fluid Mech. 578, 35–65.
Whitehead, J.A., Chapman, D.C., 1986. Laboratory observations of a gravity current on a sloping bottom: the generation of shelf waves. J. Fluid Mech. 172, 373–399.
Wright, D.G., 1989. On the alongshelf evolution of an idealized density front. J. Phys. Oceanogr. 19 (April (4)), 532–541.
Zhang, W.G., Wilkin, J.L., Levin, J.C., Arango, H.G., 2009. An adjoint sensitivity study of buoyancy- and wind-driven circulation on the new jersey inner shelf. J. Phys. Oceanogr. 39 (July (7)), 1652–1668.